Neuron

Article

Sequential transitions of male sexual behaviors driven by dual acetylcholine-dopamine dynamics

Graphical abstract

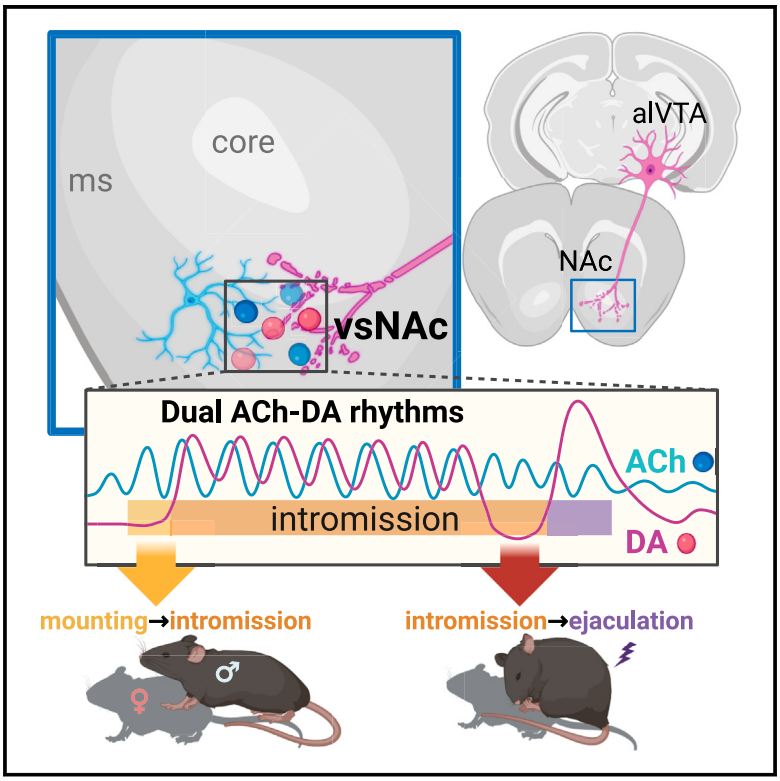

Authors

Ai Miyasaka, Takeshi Kanda, Naoki Nonaka, ..., Takeshi Sakurai, Katsuyasu Sakurai, Qinghua Liu

Correspondence

sakurai.takeshi.gf@u.tsukuba.ac.jp (T.S.), sakurai.katsuyasu.gm@u.tsukuba.ac.jp (K.S.), liuqinghua@nibs.ac.cn (Q.L.)

In brief

Miyasaka et al. identify the ventral shell of the NAc (vsNAc) as a key site where dual acetylcholine-dopamine rhythms orchestrate the transition from intromission to ejaculation. This study uncovers a brain region regulating ejaculation, extending beyond spinal mechanisms.

Highlights

- Dual ACh-DA rhythms emerge in the vsNAc during intromission
- Dual ACh-DA rhythms are generated locally via reciprocal nAChR and D2R signaling
- ChAT or D2R knockdown in the vsNAc diminishes intromission and ejaculation
- ACh release activation during intromission triggers ejaculation

Miyasaka et al., 2025, Neuron *113*, 1–19
April 16, 2025
https://doi.org/10.1016/j.neuron.2025.01.032

CellPress

Please cite this article in press as: Miyasaka et al., Sequential transitions of male sexual behaviors driven by dual acetylcholine-dopamine dynamics, Neuron (2025), https://doi.org/10.1016/j.neuron.2025.01.032

Neuron

CellPress
OPEN ACCESS

Article

Sequential transitions of male sexual behaviors driven by dual acetylcholine-dopamine dynamics

Ai Miyasaka,[1,2,3] Takeshi Kanda,[1,4,13] Naoki Nonaka,[3,13] Yuka Terakoshi,[1] Yoan Cherasse,[1] Yukiko Ishikawa,[1] Yulong Li,[5] Hotaka Takizawa,[6,7] Arisa Hirano,[1,2] Jun Seita,[3] Masashi Yanagisawa,[1,8,9] Takeshi Sakurai,[1,2,10,*] Katsuyasu Sakurai,[1,*] and Qinghua Liu[1,11,12,14,*]

[1]International Institute for Integrative Sleep Medicine, University of Tsukuba, Tsukuba, Ibaraki 305-8575, Japan
[2]Institute of Medicine, University of Tsukuba, Tsukuba, Ibaraki 305-8575, Japan
[3]Advanced Data Science Project, RIKEN Information R&D and Strategy Headquarters, RIKEN, Tokyo 103-0027, Japan
[4]Department of Neurophysiology, Nara Medical University, Kashihara, Nara 634-8521, Japan
[5]State Key Laboratory of Membrane Biology, Peking University School of Life Sciences, Beijing 100871, China
[6]Institute of Systems and Information Engineering, University of Tsukuba, Tsukuba, Ibaraki 305-8573, Japan
[7]Academic Computing and Communications Center, University of Tsukuba, Tsukuba, Ibaraki 305-8577, Japan
[8]Department of Molecular Genetics, University of Texas Southwestern Medical Center, Dallas, TX 75390, USA
[9]Life Science Center for Survival Dynamics, Tsukuba Advanced Research Alliance, University of Tsukuba, Tsukuba, Ibaraki 305-8575, Japan
[10]Life Science Center for Tsukuba Advanced Research Alliance (TARA), University of Tsukuba, Tsukuba, Ibaraki 305-8575, Japan
[11]New Cornerstone Science Laboratory, National Institute of Biological Sciences, Beijing (NIBS), Beijing 102206, China
[12]Tsinghua Institute of Multidisciplinary Biomedical Research (TIMBR), Tsinghua University, Beijing 102206, China
[13]These authors contributed equally
[14]Lead contact
*Correspondence: sakurai.takeshi.gf@u.tsukuba.ac.jp (T.S.), sakurai.katsuyasu.gm@u.tsukuba.ac.jp (K.S.), liuqinghua@nibs.ac.cn (Q.L.)
https://doi.org/10.1016/j.neuron.2025.01.032

SUMMARY

The neural mechanisms underlying the sequential transitions of male sexual behaviors, including mounting, intromission, and ejaculation, remain largely unexplored. Here, we report that acetylcholine (ACh)-dopamine (DA) dynamics in the ventral shell of the nucleus accumbens (vsNAc) regulate these sexual transitions in male mice. During intromission, the vsNAc displays a unique pattern of dual ACh-DA rhythms, generated by reciprocal regulation between ACh and DA signaling via nicotinic ACh receptors (nAChRs) and DA D2 receptors (D2Rs). Knockdown of choline acetyltransferase (ChAT) or D2R in the vsNAc diminishes the occurrence of intromission and ejaculation. Optogenetic manipulations demonstrated that DA signaling maintains sexual behaviors by suppressing $D2R^{vsNAc}$ neurons. Moreover, ACh signaling promotes the initiation of mounting and intromission and facilitates the intromission-ejaculation transition by inducing a slowdown in DA rhythm. Together, these findings reveal that coordinated ACh-DA dynamics in the vsNAc play a critical role in orchestrating the sequential transitions of male sexual behaviors.

INTRODUCTION

In mammals, males engage in a stereotypical sequence of sexual behaviors when they encounter females in estrus. This sequence of male sexual behaviors consists of courtship (appetitive) behaviors, such as sniffing and chasing, followed by copulatory (consummatory) behaviors, such as mounting, intromission, and ejaculation in rodents.[1–6] Appropriate expression of these sequential sexual behaviors is not only considered as a measure of male attractivity but also important for the successful completion of sexual behaviors.[7] It has been suggested that each sexual behavioral sequence is regulated by a distinctive neuronal mechanism. For example, the medial preoptic area (MPOA) has been implicated in copulatory behavior, while the nucleus accumbens (NAc) is thought to be involved in appetitive behavior.[1,6] However, recent studies have suggested that the MPOA controls mounting[8–11] and that the NAc may facilitate the learning and reinforcement of male sexual behaviors.[12–14] Thus, sexual behaviors represent a complex sequence of actions involving multiple brain regions working in concert. However, the neural mechanisms that govern the sequential transitions of these sexual behaviors, specifically transitions from mounting to intromission to ejaculation, remain poorly understood.

Accumulating studies have suggested that dopamine (DA) signaling functions as a primary driver for sexual motivation and behaviors.[15–22] Moreover, administration of cholinergic agonists in the preoptic area (POA) or substantia nigra altered the number or frequency of intromissions preceding ejaculation in rodents, implicating a regulatory role of acetylcholine

Please cite this article in press as: Miyasaka et al., Sequential transitions of male sexual behaviors driven by dual acetylcholine-dopamine dynamics, Neuron (2025), https://doi.org/10.1016/j.neuron.2025.01.032

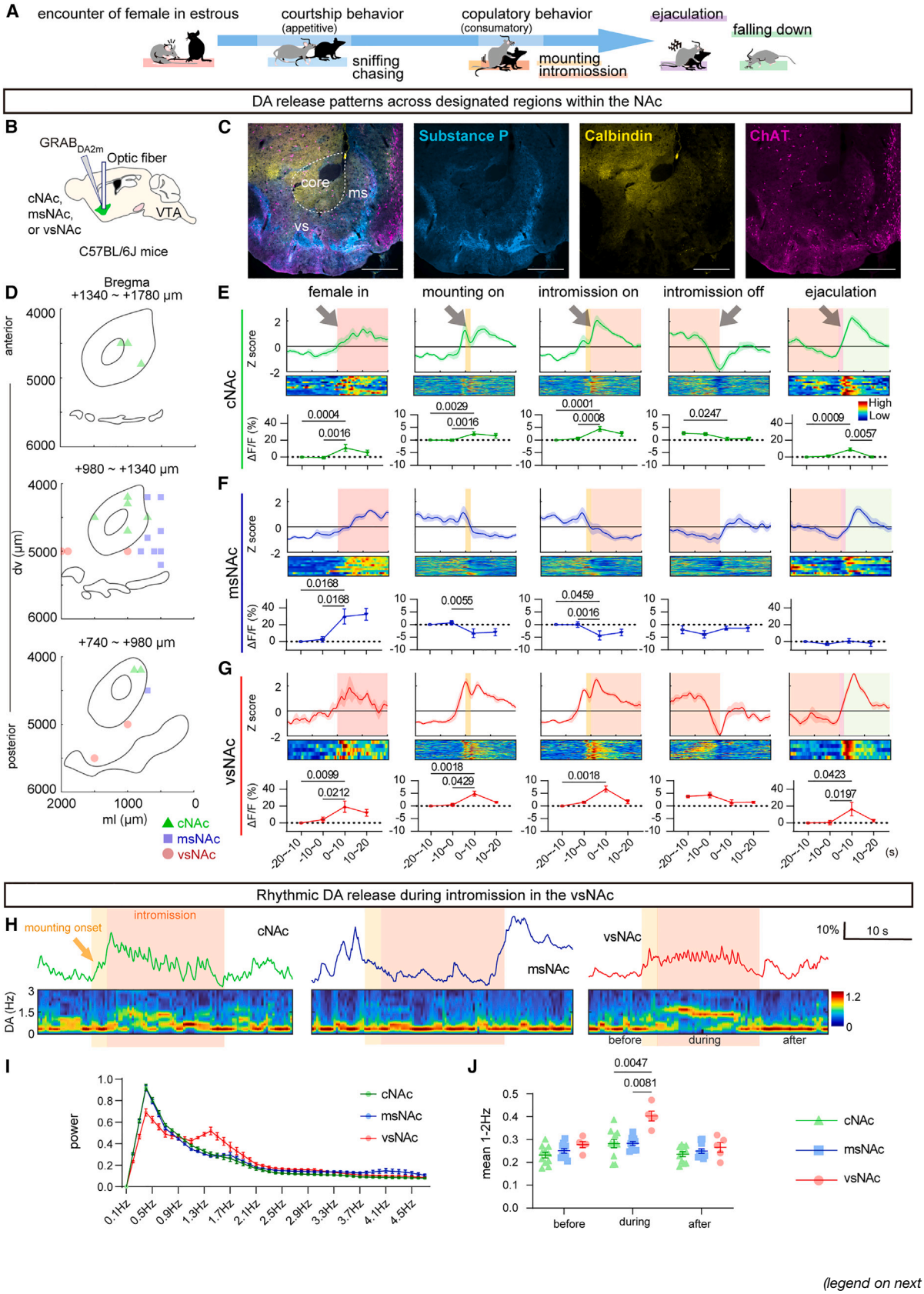

(legend on next page)

Please cite this article in press as: Miyasaka et al., Sequential transitions of male sexual behaviors driven by dual acetylcholine-dopamine dynamics, Neuron (2025), https://doi.org/10.1016/j.neuron.2025.01.032

(ACh) signaling during male copulatory behaviors.[17,23,24] However, it remains unclear where and how these neurotransmitters (NTs) interplay and regulate male sexual behaviors. Early microdialysis studies had detected an overall increase in extracellular DA in the NAc during male sexual behaviors in rats.[25–27] Recent fiber photometry studies recorded transient increases of DA levels during intromission and ejaculation in male mice using the high temporal resolution G-protein-coupled receptor activation-based $(GRAB)_{DA}$ sensor.[18–20] Because previous studies have not suggested a critical involvement of the NAc in the regulation of sexual behaviors,[28–30] the regulatory mechanism and functional significance of DA dynamics in the NAc during male sexual behaviors have not been carefully investigated.

In this study, we hypothesized that ACh signaling modulates DA dynamics in the NAc to regulate male sexual behaviors, based on recent reports that ACh signaling regulates DA release from the dopaminergic axon terminals in the striatum.[31–35] By monitoring DA dynamics in various subregions of the NAc using the $GRAB_{DA2m}$ sensor,[18,19] we found that real-time DA dynamics in the ventral shell of the NAc (vsNAc) closely aligned with the sequential transitions of sexual behaviors in male mice. Consistent with our hypothesis, we observed a unique signature of dual ACh-DA rhythms in the vsNAc during intromission. *Ex vivo* brain slice imaging and computational modeling revealed that the dual ACh-DA rhythms were generated by reciprocal regulation between ACh and DA signaling via nAChR and D2R receptors, respectively. By optogenetic manipulations of ACh and DA release into the vsNAc, we demonstrated that dual ACh and DA dynamics in the vsNAc cooperatively drive the sequential transitions of male copulatory behaviors.

RESULTS

DA dynamics in the vsNAc closely align with serial transitions of male sexual behaviors

After sniffing and chasing receptive female mice, male mice engage in repeated cycles of mounting and intromission, which culminate in ejaculation followed by a brief falling and immobile phase (Figure 1A). To study DA dynamics in the NAc during male sexual behaviors, we performed fiber photometry recording at the NAc of C57BL/6J male mice following injection with an adeno-associated virus (AAV) expressing $GRAB_{DA2m}$ sensor in neurons (Figure 1B). Since the NAc is anatomically heterogeneous,[36–40] we examined DA dynamics in different subregions of the NAc by inserting optic fibers into the core (c), medial shell (ms), or ventral shell (vs) of the NAc (Figures 1C and 1D). Both vsNAc and cNAc, but not msNAc, exhibited an increase of $GRAB_{DA2m}$ signals that corresponded to all the sequential transitions of male sexual behaviors (Figures 1E–1G). Notably, only the vsNAc, but not cNAc or msNAc, exhibited 1–2 Hz rhythmic fluctuation of $GRAB_{DA2m}$ signals during intromission, which appeared concurrent with the intromission thrust rhythm (Figures 1H–1J; Video S1). These observations identify the vsNAc as a candidate brain region where DA dynamics may regulate the sequential transitions of male sexual behaviors, especially from intromission to ejaculation.

Local regulation of DA rhythm in the vsNAc during intromission

The ventral tegmental area (VTA) comprises a heterogeneous population of dopaminergic neurons (DA^{VTA} neurons) that, depending on their genetic and anatomical characteristics, send specific axonal projections to different target regions, including the NAc.[36,38] By two-color cholera toxin B subunit (CTB)-mediated retrograde labeling, we found that the vsNAc and msNAc received projections from the anterolateral (al) and posteromedial (pm) VTA neurons, respectively (Figures S1A–S1C). To compare the activities of dopaminergic neurons in the alVTA (DA^{alVTA}) and pmVTA (DA^{pmVTA}) during male sexual behaviors, we unilaterally injected AAV-hSyn-DIO-GCaMP6s and inserted optical fibers into the alVTA or pmVTA of *DAT-ires-Cre* (DAT^{Cre}) mice (Figures S1D and S1E). Fiber photometry recording revealed that the DA^{alVTA}, but not DA^{pmVTA}, neurons exhibited GCaMP dynamics in accordance with $GRAB_{DA2m}$ dynamics in the vsNAc during male sexual behaviors (Figures S1F–S1H). However, we did not observe rhythmic fluctuation of GCaMP signals in the DA^{alVTA} or DA^{pmVTA} neurons during intromission (Figure S1F).

We also performed fiber photometry to monitor the neuronal activity in the vsNAc-projecting dopaminergic ($DA^{VTA\rightarrow vsNAc}$) axon terminals by injecting AAV-hSyn-DIO-GCaMP6s into the VTA and inserting optical fibers into the vsNAc of DAT^{Cre} mice (Figure S1I). Unlike the neuronal activity in the somata of the DA^{alVTA} neurons, the GCaMP dynamics in the $DA^{VTA\rightarrow vsNAc}$ axons were similar to $GRAB_{DA2m}$ dynamics in the vsNAc, in terms of both high signal intensity and rhythmic fluctuations

Figure 1. DA dynamics in the vsNAc closely align with serial transitions of male sexual behaviors

(A) Schematic demonstrating sequential sexual behaviors in male mice.

(B) Schematic demonstrating fiber photometry recording of $GRAB_{DA2m}$ signals in the vsNAc of C57BL/6J mice.

(C) Representative images showing immunostaining of substance P, calbindin, and ChAT in the NAc and surrounding regions (scale bar, 500 μm).

(D) Schematic demonstrating recording sites of $GRAB_{DA2m}$ imaging in various NAc subregions.

(E–G) Top: peri-event time plot (PETP) of *Z* scored ΔF/F of $GRAB_{DA2m}$ signals around each transition of male sexual behavior in the cNAc (E, $n = 11$ mice), msNAc (F, $n = 10$ mice), and vsNAc (G, $n = 5$ mice). Middle: heatmap of PETP with individual events/row. Bottom: mean ΔF/F of $GRAB_{DA2m}$ every 10 s in each behavioral event.

(H) Representative traces of $GRAB_{DA2m}$ dynamics during intromission and spectrum band calculated by FFT analysis in the cNAc (left), msNAc (center), and vsNAc (right).

(I) Power spectrum of DA dynamics during intromission in the vNAc, msNAc, and vsNAc.

(J) Mean power spectrum of 1–2 Hz frequency of DA dynamics before, during, and after intromission in the cNAc, msNAc, and vsNAc.

Mean ± SEM.

See also Figure S1, Table S1, and Video S1.

Please cite this article in press as: Miyasaka et al., Sequential transitions of male sexual behaviors driven by dual acetylcholine-dopamine dynamics, Neuron (2025), https://doi.org/10.1016/j.neuron.2025.01.032

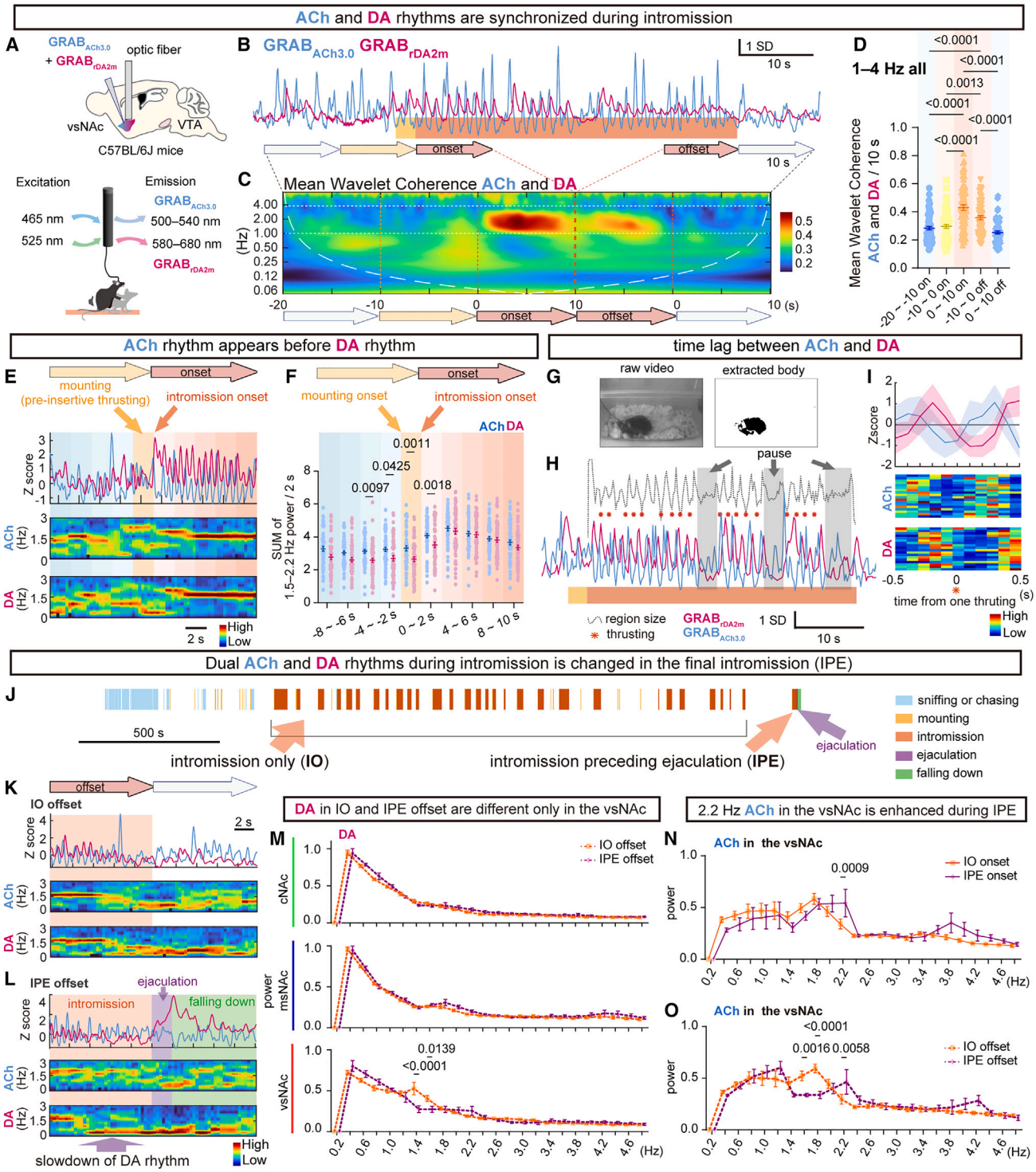

Figure 2. Dual ACh-DA rhythms are observed in the vsNAc during intromission

(A) Strategy for simultaneous fiber photometry recordings of ACh and DA dynamics in the vsNAc.

(B) Representative traces of $GRAB_{ACh3.0}$ and $GRAB_{rDA2m}$ before, during, and after intromission.

(C) Heatmap plot of mean wavelet coherence between $GRAB_{ACh3.0}$ and $GRAB_{rDA2m}$ dynamics around the extracted 50 s intromission.

(D) Comparison of 1–4 Hz wavelet coherence between $GRAB_{ACh3.0}$ and $GRAB_{rDA2m}$ among every 10 s around intromission.

(E) Representative *Z* scored traces of $GRAB_{ACh3.0}$ and $GRAB_{rDA2m}$ in the vsNAc (top). Heatmap showing the power spectrum processed by the FFT analysis of $GRAB_{ACh3.0}$ (center) and $GRAB_{rDA2m}$ (bottom) around intromission onset.

(legend continued on next page)

Please cite this article in press as: Miyasaka et al., Sequential transitions of male sexual behaviors driven by dual acetylcholine-dopamine dynamics, Neuron (2025), https://doi.org/10.1016/j.neuron.2025.01.032

during intromission (Figures S1J and S1K). We confirmed that the rhythmic GCaMP signals in the vsNAc reflected real neuronal activity rather than motion artifacts during intromission by recording the 405 nm isosbestic GCaMP control signals (Figure S1K). These observations suggest that DA dynamics in the vsNAc are regulated locally within the vsNAc.

Dual ACh-DA rhythms in the vsNAc during intromission

By immunohistochemistry of choline acetyltransferase (ChAT) in DAT^{Cre} mice, in which DA neurons were marked by GFP expression, we confirmed the existence of cholinergic interneurons in the vsNAc ($ChAT^{vsNAc}$) in proximity to the $DA^{VTA \rightarrow vsNAc}$ axons (Figures S2A–S2C). To test our hypothesis that ACh signaling regulates DA dynamics in the vsNAc during male sexual behaviors, we performed dual fiber photometry to simultaneously monitor ACh and DA dynamics after AAV-mediated expression of green fluorescent $GRAB_{ACh3.0}$[41] and red fluorescent $GRAB_{rDA2m}$[42] in the vsNAc of C57BL/6J male mice (Figures 2A–2L). Accordingly, we observed a specific signature of dual ACh and DA rhythms during intromission (Figure 2B; Video S2). Fiber photometry recording revealed that both the neuronal activity of $ChAT^{vsNAc}$ neurons (Figures S2D–S2F) and ACh release in the vsNAc (Figures S2G–S2I) were rhythmic during intromission, suggesting that the rhythmic activity of $ChAT^{vsNAc}$ neurons may regulate the rhythmic release of ACh and possibly DA in the vsNAc during intromission.

By wavelet coherence analysis, we found that the coherence between ACh and DA rhythms in the 1–4 Hz band was significantly increased during intromission (Figures 2C, 2D, and S2J). Fast Fourier transform (FFT) analysis further revealed a strong, continuous 1.5–2.2 Hz band present in both ACh and DA rhythms during intromission (Figures 2E, 2K, and 2L). This distinct frequency band was absent in either the pre- or post-intromission phase, suggesting a unique signature of dual ACh-DA rhythms specific to the intromission period (Figures 2E and 2K). Moreover, the ACh rhythm, but not the DA rhythm, appeared just before the onset of intromission: the 1.5–2.2 Hz power of the ACh rhythm was continuously higher than that of DA rhythm from 6 s before to 2 s after the intromission onset, including the pre-insertive thrusting period (mounting) (Figure 2F). By contrast, for mounting-only events, the 1.5–2.2 Hz power of the ACh rhythm was intermittently higher than that of DA rhythm around the mounting onset (Figures S2K and S2L). These observations suggest that the 1.5–2.2 Hz ACh rhythm plays a critical role in the mounting-to-intromission transition.

To measure the time lag between ACh and DA rhythms during intromission, we compared the ACh/DA rhythm with the pelvic thrust rhythm by analyzing the dynamic changes in the body size of male and female mice in the video (Figures 2G and 2H). By plotting the ACh and DA rhythms around each pelvic thrusting event, we found the trough of the ACh rhythm was approximately 0.1 s before, whereas that of the DA rhythm was ~0.1–0.2 s after the thrusting (Figure 2I). Moreover, the ACh rhythm, but not the DA rhythm, persisted during the short pauses of pelvic thrusting during long intromissions (Figure 2H). Taken together, these observations suggest that the ACh rhythm may act as the primary driver in generating the dual ACh-DA rhythm during intromission (Figures 2E–2I).

Signatures of the intromission preceding ejaculation

During a successful cycle of sexual behaviors, most intromissions do not result in ejaculation (intromission only [IO]), whereas the final intromission typically precedes ejaculation (intromission preceding ejaculation [IPE]) (Figure 2J). Interestingly, the coherence of the dual ACh-DA rhythms was significantly enhanced at the intromission onset of IPE relative to IO (Figures S2M and S2N). While the 1.5–2.2 Hz ACh-DA rhythms continued until the termination of IO (Figure 2K), there was a specific slowdown of the 1.5–2.2 Hz DA rhythm just before ejaculation that coincided with the big surge of DA release in the IPE (Figure 2L). Importantly, this brief suppression of DA rhythm was observed only in the vsNAc, but not in the msNAc or cNAc, at the IPE offset (Figure 2M), suggesting that it may be a prerequisite for the intromission-to-ejaculation transition. Moreover, the ACh rhythm at IPE onset displayed stronger 2.2 Hz power than that at IO onset (Figure 2N). At IPE offset, the 1.6–2.0 Hz power of the ACh rhythm was notably lower, while the 2.2 Hz power was significantly higher than that at IO offset (Figure 2O). These observations suggest the possibility that the 2.2 Hz ACh rhythm may lead to a slowdown of the DA rhythm to facilitate the transition from intromission to ejaculation.

Detailed analysis of ACh-DA rhythms in relation to characteristics of sexual behavior

To examine whether the dual ACh-DA rhythms are modulated by sexual experience, we subjected naive male mice to weekly sexual behavior tests to observe the effect of sexual experience. By comparing ACh-DA coherence among the first, second, and third tests, we observed a progressive decrease in 1–4 Hz ACh-DA coherence with an increasing number of sexual tests (Figure S2O), suggesting that the ACh-DA rhythms were

(F) Comparison of the total amounts of 1.5–2.2 Hz power of $GRAB_{ACh3.0}$ and $GRAB_{rDA2m}$ collected every 2 s around intromission onset.
(G) Thrusting was determined by the region size change of the extracted male and female mice.
(H) Representative *Z* scored traces of $GRAB_{ACh3.0}$ and $GRAB_{rDA2m}$ in the vsNAc and region size of the extracted body. Orange stars mark the pelvic thrusts.
(I) Average traces (top) and heatmap plot (bottom) of $GRAB_{ACh3.0}$ and $GRAB_{rDA2m}$ around the pelvic thrusts during intromission.
(J) Representative illustration of sexual behavior (left). Behavioral ethograms for Figure 2 (right).
(K and L) Same as (E), FFT analyses around IO offset (K) and IPE offset (L).
(M) Power spectrum of $GRAB_{DA2m}$ in the cNAc (top, $n = 11$ mice/group), msNAc (middle, $n = 10$ mice/group), and vsNAc (bottom, $n = 5$ mice/group) during 10 s offset of IO and IPE. Two-way ANOVA with Šídák's test over IO and IPE offset for every 0.2 Hz.
(N and O) Same as (M), power spectrum of $GRAB_{ACh3.0}$ in the vsNAc during 10 s onset of IO and IPE (N) and during 10 s offset of IO and IPE (O) ($n = 4$ mice/group). Two-way ANOVA analysis with Šídák's test between IO and IPE onset for every 0.2 Hz (N) and between IO and IPE offset for every 0.2 Hz (O).
Mean ± SEM.
See also Figure S2, Table S1, and Video S2.

Please cite this article in press as: Miyasaka et al., Sequential transitions of male sexual behaviors driven by dual acetylcholine-dopamine dynamics, Neuron (2025), https://doi.org/10.1016/j.neuron.2025.01.032

somehow modulated by sexual experience. We also compared the 1–4 Hz coherence among short, medium, and long intromission epochs to examine the potential relationship between the ACh-DA coherence and intromission length. Notably, the 1–4 Hz coherence was significantly stronger in long intromissions (>30 s) than in short (<10 s) and medium (10–30 s) intromissions (Figure S2P, bottom), suggesting a potential link between ACh-DA coherence and intromission length. However, no significant difference was observed in ACh-DA coherence between sessions with a large number of intromission bouts ($\geq$8 bouts) and those with a small number of bouts (<8 bouts) (Figure S2P, top), indicating that the coherence of dual ACh-DA rhythms is independent of the number of intromission bouts.

ACh signaling regulates DA release in the vsNAc

To examine whether ACh signaling could regulate DA release in the vsNAc, we first confirmed the presence of $ChAT^{vsNAc}$ interneurons by AAV-mediated Cre-dependent GFP expression in the vsNAc of *ChAT*^{Cre} mice (Figures S3A and S3B). Notably, the $ChAT^{vsNAc}$ interneurons project to only the vsNAc, but not to cNAc and msNAc. Next, we injected AAV-Syn-FLEX-ChrimsonR and AAV-hSyn-$GRAB_{DA2m}$ into the vsNAc of *ChAT*^{Cre} mice, followed by *ex vivo* NAc brain slice imaging coupled with optogenetics and pharmacological manipulations (Figures 3A–3C). Optogenetic activation of $ChAT^{vsNAc}$ neurons evoked an immediate and robust increase of $GRAB_{DA2m}$ signals in the NAc slices (Figures 3B and 3C). This cholinergic stimulation of DA release was suppressed by dihydro-β-erythroidine hydrobromide (DhβE)-nAChR antagonist—at all frequencies (Figures 3B and 3C). Interestingly, an mAChR antagonist, atropine, suppressed cholinergic activation of DA release during 20 or 40 Hz opto-stimulation of $ChAT^{vsNAc}$ neurons but induced a sharp increase of DA release during 1 or 10 Hz opto-stimulation of $ChAT^{vsNAc}$ neurons, possibly owing to the disinhibition of mAChR-mediated suppression of ACh release (Figures 3B and 3C).[43] *In situ* hybridization revealed the expression of all five mAChR1–5 (*Chrm1–5*) in the majority of $ChAT^{vsNAc}$ neurons and mAChR1–5 in the DA^{VTA} neurons (Figures S3C–S3F). Expression of nAChR has also been detected in the DA^{VTA} neurons.[44] These results suggest that ACh signaling promotes DA release via nAChR signaling but also inhibits DA release in some contexts via mAChR signaling in the vsNAc.

DA signaling reciprocally regulates ACh release in the vsNAc

To examine whether DA signaling reciprocally regulates the activity of $ChAT^{vsNAc}$ neurons, we performed *ex vivo* Ca^{2+} imaging in the NAc slices following injection of AAV-Syn-FLEX-ChrimsonR into the VTA and AAV-hSyn-DIO-GCaMP6s into the vsNAc of *ChAT*^{Cre};*DAT*^{Cre} mice (Figures 3A, 3D, and 3E). Optogenetic (1 Hz) stimulation of $DA^{VTA\rightarrow NAc}$ axons evoked different responses in the $ChAT^{NAc}$ neurons, with ~20% increasing, ~30% decreasing, and ~50% exhibiting no change in intracellular Ca^{2+} levels (Figure 3E). By contrast, higher-frequency ($\geq$10 Hz) stimulation of $DA^{VTA\rightarrow NAc}$ axons increased the activity of ~40% $ChAT^{NAc}$ neurons and decreased the activity of ~30% $ChAT^{NAc}$ neurons (Figure 3E). Notably, a small subset of $ChAT^{NAc}$ neurons displayed rhythmic fluctuation of intracellular Ca^{2+} levels in the NAc slices (Figure 3D; Video S3), which was consistent with the rhythmic fluctuation of Ca^{2+} levels in $ChAT^{vsNAc}$ neurons and rhythmic release of ACh in the vsNAc observed by *in vivo* fiber photometry during intromission (Figures S2D–S2I).

The existence of both *Drd1*$^{+}$ChAT^{+} and *Drd2*$^{+}$ChAT^{+} neurons in the vsNAc (Figures 3F and 3G) raised two potential mechanisms for the regulation of $ChAT^{vsNAc}$ neurons by DA signaling: (1) inhibition of $ChAT^{vsNAc}$ neurons via D2R-mediated Gi/o signaling and (2) activation of $ChAT^{vsNAc}$ neurons via D1R-mediated Gs signaling.[45] To prove these possibilities, we injected AAV-Syn-FLEX-ChrimsonR and AAV-hSyn-$GRAB_{ACh3.0}$ into the vsNAc of *ChAT*^{Cre} mice (Figures 3A and 3H–3K). Optogenetic activation of $ChAT^{NAc}$ neurons increased $GRAB_{ACh3.0}$ signals in the NAc slices, which was suppressed by a D2R agonist, bromocriptine, under all stimulation conditions except for 40 Hz stimulation (Figures 3H and 3I). Thus, the D2R-mediated inhibition of $ChAT^{NAc}$ neurons could suppress ACh release from $ChAT^{NAc}$ neurons following $\leq$20 Hz optogenetic stimulation (Figure 3I). Next, we investigated whether ACh release was also modulated by D1R signaling in the NAc slices by bath application of a D1R agonist, SKF38398. Activation of D1R signaling caused distinct changes in ACh release in the NAc, with 12.1% increasing, 50.4% decreasing, and 37.5% exhibiting no change in $GRAB_{ACh3.0}$ signals (Figures 3J and 3K). Taken together, these results suggest the reciprocal regulation of ACh release by DA signaling in the vsNAc, which is potentially mediated by both D1R and D2R expressed on $ChAT^{vsNAc}$ neurons.

Modeling of dual ACh-DA rhythms by reciprocal regulation between ACh and DA signaling

To further study how the dual ACh-DA rhythms were generated by reciprocal regulation between ACh and DA in the vsNAc during intromission, we performed computational modeling using a simplified neuronal assemblage consisting of the dopaminergic ($DA^{VTA\rightarrow vsNAc}_{sim}$) axon terminals, cholinergic neurons ($ChAT^{vsNAc}_{sim}$), and the extracellular environment (Figures 4A and S4A–S4D). In this modeling, we defined the release probability measurement (*RPM*) of the neuronal assemblage as a measure of the intensity of neuronal activity (Figure 4B). We set *Activation* to mimic the spontaneous firing of each neuronal assemblage or stimulation by other neurons (Figure S4A). Additionally, the *Receptor* function represents the effect of each receptor upon binding of ACh or DA (Figure 4B). Both *Activation* and *Receptor* constantly change the *RPM* that determines the volume of NT released to the extracellular environment (Figures 4B and S4A).

The binding of DA to different DA receptors activates distinct intracellular G protein signaling to regulate neuronal activity: D1R triggers Gs signaling to activate neuronal activity, whereas D2R activates G protein gates inwardly rectifying potassium (GIRK) channels-mediated signaling to inhibit neuronal activity.[45–47] On the other hand, the binding of ACh to nAChR causes a rapid influx of cations, such as Na^{+} and Ca^{2+}, to activate neuronal activity.[48,49] We hypothesized that the characteristics of each receptor consist of two axes: the effect intensity (effect: *RE*) with which the receptor changes neuronal activity and the processing speed (speed: *RS*) of the receptor in affecting the neuronal activity upon binding of ACh or DA (Figure 4B).

Please cite this article in press as: Miyasaka et al., Sequential transitions of male sexual behaviors driven by dual acetylcholine-dopamine dynamics, Neuron (2025), https://doi.org/10.1016/j.neuron.2025.01.032

CellPress
OPEN ACCESS

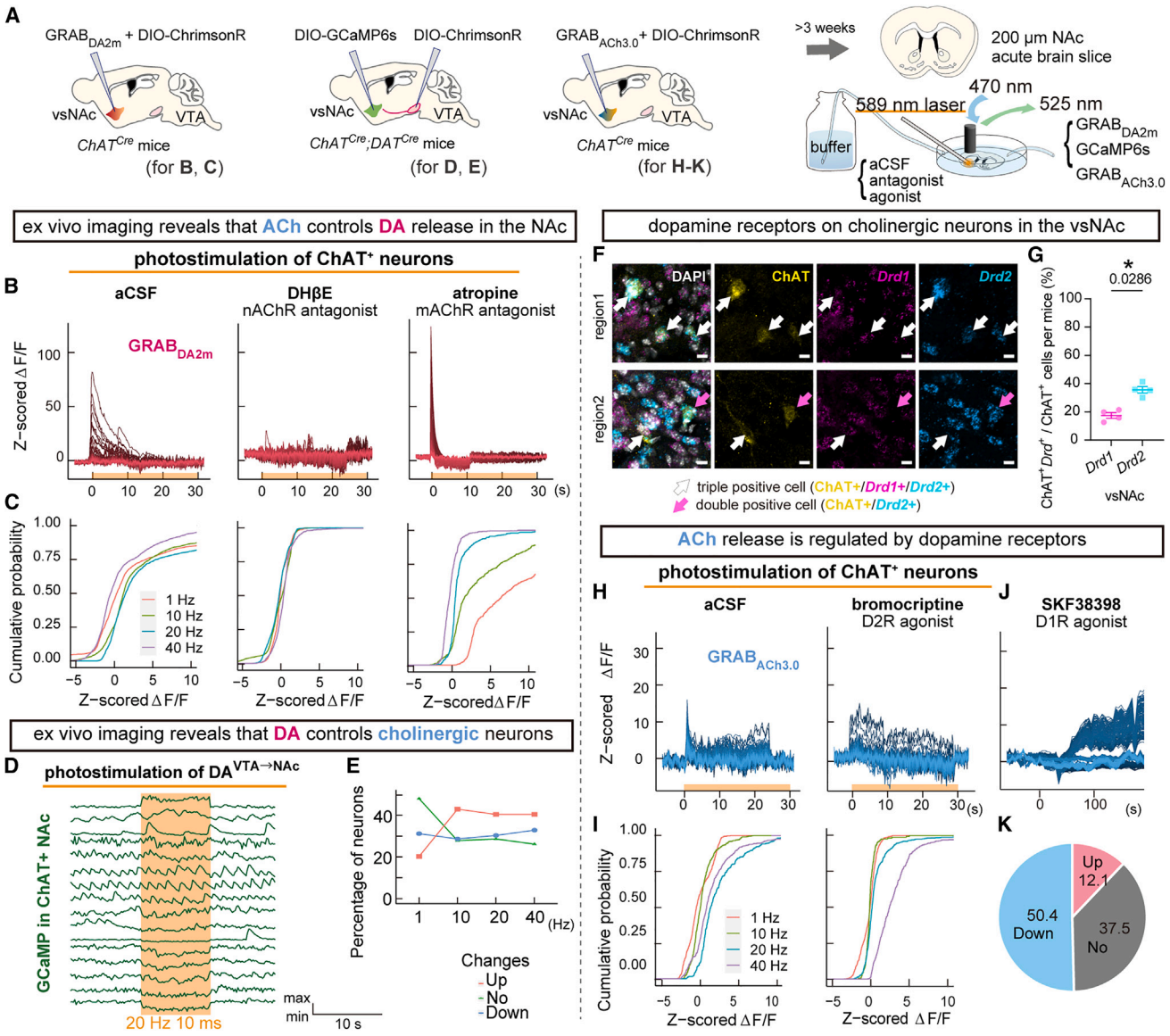

Figure 3. *Ex vivo* NAc brain slice imaging reveals mutual regulation of ACh and DA signaling

(A) Schematic of *ex vivo* NAc brain slice imaging experiments.

(B and C) Optogenetic stimulation of $ChAT^{NAc}$ neurons with ChrimsonR and imaging of DA with $GRAB_{DA2m}$. Representative traces of *Z* scored ΔF/F of $GRAB_{DA2m}$ signals upon 10 ms photostimulation at 20 Hz for 30 s (bottom orange bars) in the absence of AChR antagonists (left) or in the presence of 1 μM DHβE (center) or 2 μM atropine (right). Individual lines indicate the signals from each ROI (B). Cumulative probability plots of mean *Z* scored ΔF/F of $GRAB_{DA2m}$ signals for 30 s after the onset of photostimulation. *n* = 2,332 (left), 776 (center), and 570 (right) regions of interest (ROIs) at any photostimulation frequency. Individual lines of different colors show the signals at different photostimulation frequencies (C).

(D and E) Optogenetic stimulation of $DA^{VTA\rightarrow NAc}$ axons and Ca^{2+} imaging with GCaMP. Representative traces of GCaMP signals upon 10 ms photostimulation at 20 Hz for 10 s (D). Classification of $ChAT^{NAc}$ neurons by different response to photostimulation. *n* = 181 cells (E). See also Video S3.

(F and G) Representative images showing co-expression of ChAT protein with *Drd1* and *Drd2* mRNA in the vsNAc (scale bars, 10 μm) (F). The percentage of $ChAT^{+}$ neurons that co-express *Drd1* or *Drd2* (G). Mean ± SEM. See Table S1.

(H and I) Optogenetic stimulation of $ChAT^{NAc}$ neurons with ChrimsonR and imaging of ACh with $GRAB_{ACh3.0}$. Representative traces of *Z* scored ΔF/F of $GRAB_{ACh3.0}$ signals upon 10 ms photostimulation at 20 Hz for 30 s in the absence of D1R and D2R agonists (left) or in the presence of 15 μM bromocriptine (right) treatment (H). Cumulative probability plots of mean *Z* scored ΔF/F of $GRAB_{ACh3.0}$ signals for 30 s after the onset of photostimulation. *n* = 657 (1 Hz), 490 (10 Hz), 325 (20 Hz), and 654 (40 Hz) ROIs (left); *n* = 657 (1 Hz), 165 (10 Hz), 654 (20 Hz), and 489 (40 Hz) ROIs (right) (I).

(J and K) $GRAB_{ACh3.0}$ imaging during bath application of a D1R agonist with $GRAB_{ACh3.0}$ imaging. All traces of *Z* scored ΔF/F of $GRAB_{ACh3.0}$ signals upon bath application of 100 μM SKF38398. Time 0 indicates the onset of the application (J). Pie chart of the response pattern of the ROI. *n* = 685 ROIs (K).

Please cite this article in press as: Miyasaka et al., Sequential transitions of male sexual behaviors driven by dual acetylcholine-dopamine dynamics, Neuron (2025), https://doi.org/10.1016/j.neuron.2025.01.032

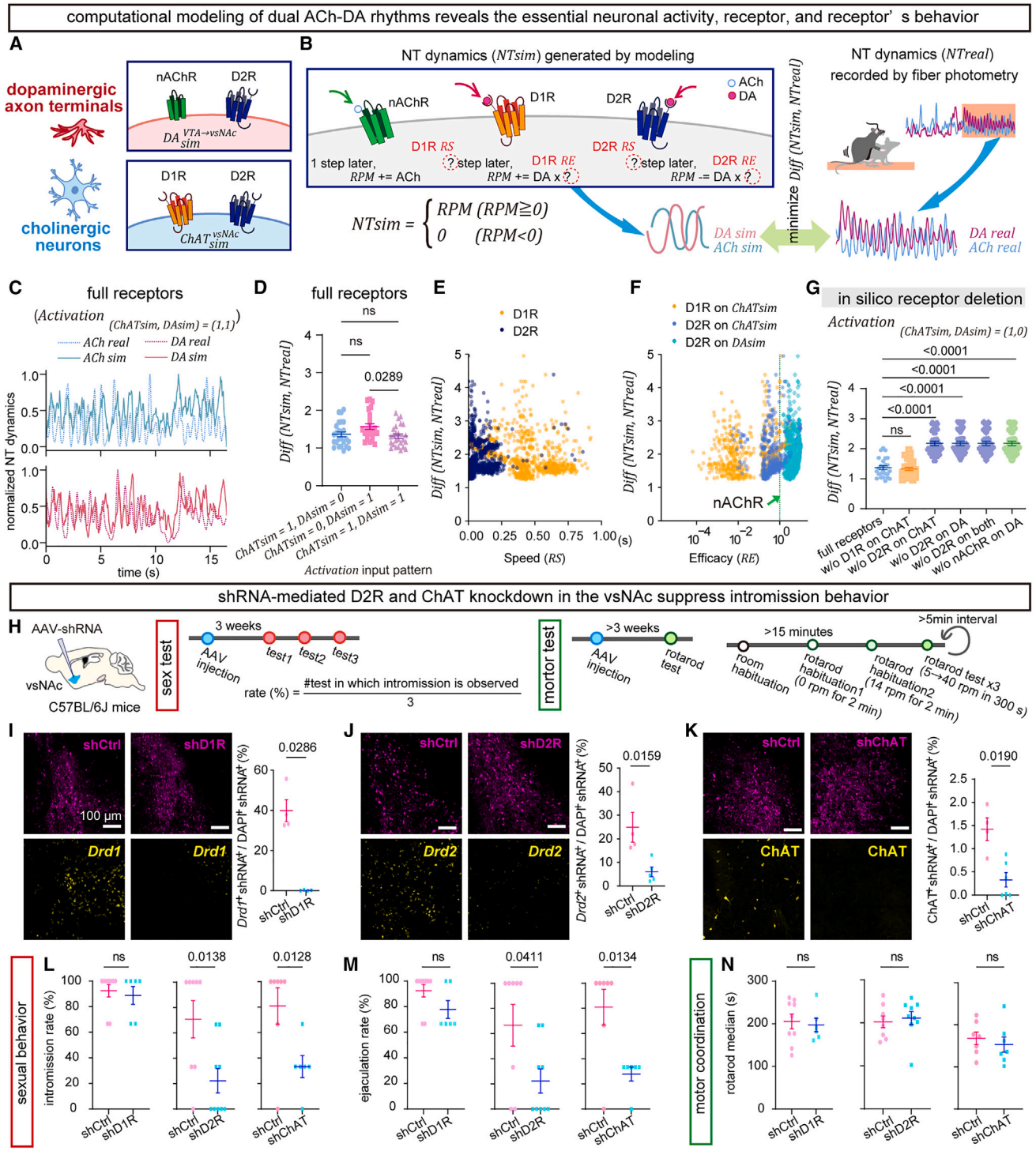

Figure 4. Computational modeling reveals that nAChR and D2R signaling are necessary for the generation of dual ACh-DA rhythms

(A–G) Computational modeling of dual ACh-DA rhythms.

(A) Setting of receptors distribution in the model.

(B) Schematic representation of the model. *RPM*, release probability measurement; *RS*, receptor speed; *RE*, receptor efficacy.

(C) Representative traces of NT_{sim} and NT_{real} of ACh and DA under the full receptor distribution.

(D) Comparison of $Diff(NT_{sim}, NT_{real})$ with four full receptors under three activation conditions; only $ChAT_{sim}^{vsNAc}$, only $DA_{sim}^{VTA\rightarrow vsNAc}$, both $ChAT_{sim}^{vsNAc}$ and $DA_{sim}^{VTA\rightarrow vsNAc}$.

(E) Comparison of $Diff(NT_{sim}, NT_{real})$ with four full receptors vs. *RS* (Receptor speed) of D1R and D2R during the generation of dual ACh-DA rhythms.

(legend continued on next page)

Please cite this article in press as: Miyasaka et al., Sequential transitions of male sexual behaviors driven by dual acetylcholine-dopamine dynamics, Neuron (2025), https://doi.org/10.1016/j.neuron.2025.01.032

Cholinergic activation is required for modeling dual ACh-DA rhythms

The goal of the modeling is to estimate the *RE* and *RS* values of each receptor to minimize the $Diff(NT_{sim}, NT_{real})$, i.e., the difference between simulated signals (NT_{sim}) and experimentally recorded *in vivo* GRAB signals (NT_{real}). Based on previous[50] and current results (Figures 3 and S3), we placed D1R and D2R on $ChAT^{vsNAc}_{sim}$ neurons and nAChR and D2R on $DA^{VTA\rightarrow vsNAc}_{sim}$ axon terminals in this model (Figure 4A). Importantly, we found that the simulated dual ACh-DA rhythms closely resembled the experimentally recorded ACh-DA rhythms (Figure 4C). To investigate the relative contributions of $ChAT^{vsNAc}_{sim}$ neurons and $DA^{VTA\rightarrow vsNAc}_{sim}$ axon terminals, we compared the $Diff(NT_{sim}, NT_{real})$ in three activation patterns: $ChAT^{vsNAc}_{sim}$ and $DA^{VTA\rightarrow vsNAc}_{sim}$ ($Activation_{(1,1)}$), only $ChAT^{vsNAc}_{sim}$ ($Activation_{(1,0)}$), and only $DA^{VTA\rightarrow vsNAc}_{sim}$ ($Activation_{(0,1)}$) (Figure S4A). The similarity between NT_{real} and NT_{sim} rhythms suggested that the $Activation_{(1,1)}$ and $Activation_{(1,0)}$ conditions were much better than the $Activation_{(0,1)}$ condition to simulate dual ACh-DA rhythms (Figure 4D). These observations suggest that the activation of cholinergic neurons is necessary to generate dual ACh-DA rhythms.

D2R, but not D1R, is required for modeling dual ACh-DA rhythms

We visualized the explored values of the *RS* and *RE* for each assumed receptor during the simulation. Notably, the *RS* of D2R was in the range of 5–50 ms, while the *RS* of D1R was approximately 350–400 ms (Figure 4E). Thus, the processing speed of D2R is approximately 7- to 80-fold faster than that of D1R in our model, which is consistent with the fact that GIRK-mediated D2R signaling is much faster than Gs-mediated D1R signaling. Moreover, the *RE* of D1R or D2R on $ChAT^{vsNAc}_{sim}$ neurons is approximately 1/100 or 1/50 of that of nAChR on $DA^{VTA\rightarrow vsNAc}_{sim}$ axon terminals, respectively. By contrast, the *RE* of D2R on $DA^{VTA\rightarrow vsNAc}_{sim}$ axon terminals is 2 to 4 times of that of nAChR (Figure 4F) and, thus, is hundreds fold larger than that of D2R on $ChAT^{vsNAc}_{sim}$ neurons in our model.

To determine the receptors essential for generating the dual ACh-DA rhythms, we performed simulations to evaluate the similarity between NT_{sim} and NT_{real} following *in silico* ablation of each receptor(Figures 4G, S4E, and S4F). Consistent with the estimation that D2R has a larger *RE* than D1R, the ablation of D2R, but not D1R, on $ChAT^{vsNAc}_{sim}$ neurons worsened the $Diff(NT_{sim}, NT_{real})$ as compared with the full receptor condition (Figure 4G). Similarly, the ablation of D2R or nAChR on $DA^{VTA\rightarrow vsNAc}_{sim}$ axon terminals significantly decreased the similarity between NT_{sim} and NT_{real}. These observations underscore the importance of the D2R-mediated DA signaling and nAChR-mediated ACh signaling in the generation of dual ACh-DA rhythms.

Knockdown of D2R and ChAT in the vsNAc diminishes intromission and ejaculation

To validate our simulation results *in vivo*, we performed RNAi-mediated knockdown of D1R, D2R, or ChAT expression by injecting AAV expressing short hairpin RNA (shRNA) targeting *Drd1* (shD1R), *Drd2* (shD2R), or *Chat* (shChAT) mRNA into the vsNAc of male mice (Figures 4H–4N and S5). Consistent with the simulation results of *in silico* receptor ablation (Figure 4G), shD2R or shChAT, but not shD1R, expression in the vsNAc diminished the frequency of intromission and ejaculation, relative to the scrambled shRNA (shCtrl)-expressing mice (Figures 4L and 4M). Moreover, shD2R or shChAT prolonged the average latency of mounting, intromission, and ejaculation (Figures S5G, S5J, and S5M), while shD2R reduced the average number of bouts and total duration of mounting and intromission (Figures S5H, S5I, S5K, and S5L). Importantly, neither shD2R nor shChAT knockdown affected the motor coordination of the mice as measured by the rotarod test (Figure 4N), excluding the possibility that male sexual behaviors were indirectly affected by impairing motor coordination. These results indicate that both ACh and DA signaling play important roles in male copulatory behaviors. Based on the results of *ex vivo* brain slice imaging, computational modeling, and RNAi knockdown experiments, we concluded that the dual ACh-DA rhythms are likely generated in the vsNAc through reciprocal ACh-DA regulations mediated by nAChR and D2R signaling in $DA^{VTA\rightarrow vsNAc}$ axon terminals and D2R signaling in $ChAT^{vsNAc}$ neurons.

A high level of DA signaling in the vsNAc is important for the maintenance of intromission

A high level of extracellular DA was observed in the vsNAc, and only the vsNAc exhibited the 1.5–2.2 Hz DA rhythm during intromission (Figure 1). To examine whether DA signaling plays a

(F) Comparison of $Diff(NT_{sim}, NT_{real})$ with four full receptors vs. *RE* (Receptor efficacy) of D1R and D2R in $ChAT^{vsNAc}_{sim}$ and D2R in $DA^{VTA\rightarrow vsNAc}_{sim}$ during the generation of dual ACh-DA rhythms. The *RE* of nAChR is shown as a green dashed line.
(G) Comparison of $Diff(NT_{sim}, NT_{real})$ under activation-only $ChAT^{vsNAc}_{sim}$ with each receptor deleted condition .
(D–G) $n = 25$ NT_{real} signals from 3 mice.
(H–N) Knockdown of ChAT or D2R, but not D1R, expression in the vsNAc diminished male sexual behavior.
(H) Schematic for AAV-shRNA-mediated target gene knockdown (left) and experimental schedule of sexual behavior tests (center) and rotarod tests (right).
(I–K) Representative images showing AAV-shD1R (I), AAV-shD2R (J), or AAV-shChAT (K) injected vsNAc region (left). Expressions of shRNA-mCherry (top) and each target gene (*Drd1* in I and *Drd2* in J) or protein (ChAT in K) (bottom), the monochromatic images of Figures S5A[1]–S5F[1]. Scale bars, 50 μm. Quantification of knockdown efficiency of D1R (I, $n = 4$ mice/group), D2R (J, $n = 5$ mice/group), and ChAT (K, $n = 6$ mice/group) (right). Knockdown score = (# $shRNA^+[D1R^+$ in I, $D2R^+$ in J, and $ChAT^+$ in K]) cells/(# $shRNA^+DAPI^+$).
(L–N) The effects of knockdown of D1R ($n = 9$ shCtrl vs. 6 shD1R mice), D2R ($n = 8$ shCtrl vs. 9 shD2R mice), or ChAT ($n = 7$ shCtrl vs. 6 or 7 shChAT mice) expression on the rate of intromission (L) and ejaculation (M) as well as the motor coordination scored by the median duration of rotarod test (N).
(L) Intromission rate (%) = (# tests in which intromission was observed)/3.
(M) Ejaculation rate (%) = (# tests in which ejaculation was observed)/3.
Mean ± SEM.
See also Figures S4 and S5 and Table S1.

Please cite this article in press as: Miyasaka et al., Sequential transitions of male sexual behaviors driven by dual acetylcholine-dopamine dynamics, Neuron (2025), https://doi.org/10.1016/j.neuron.2025.01.032

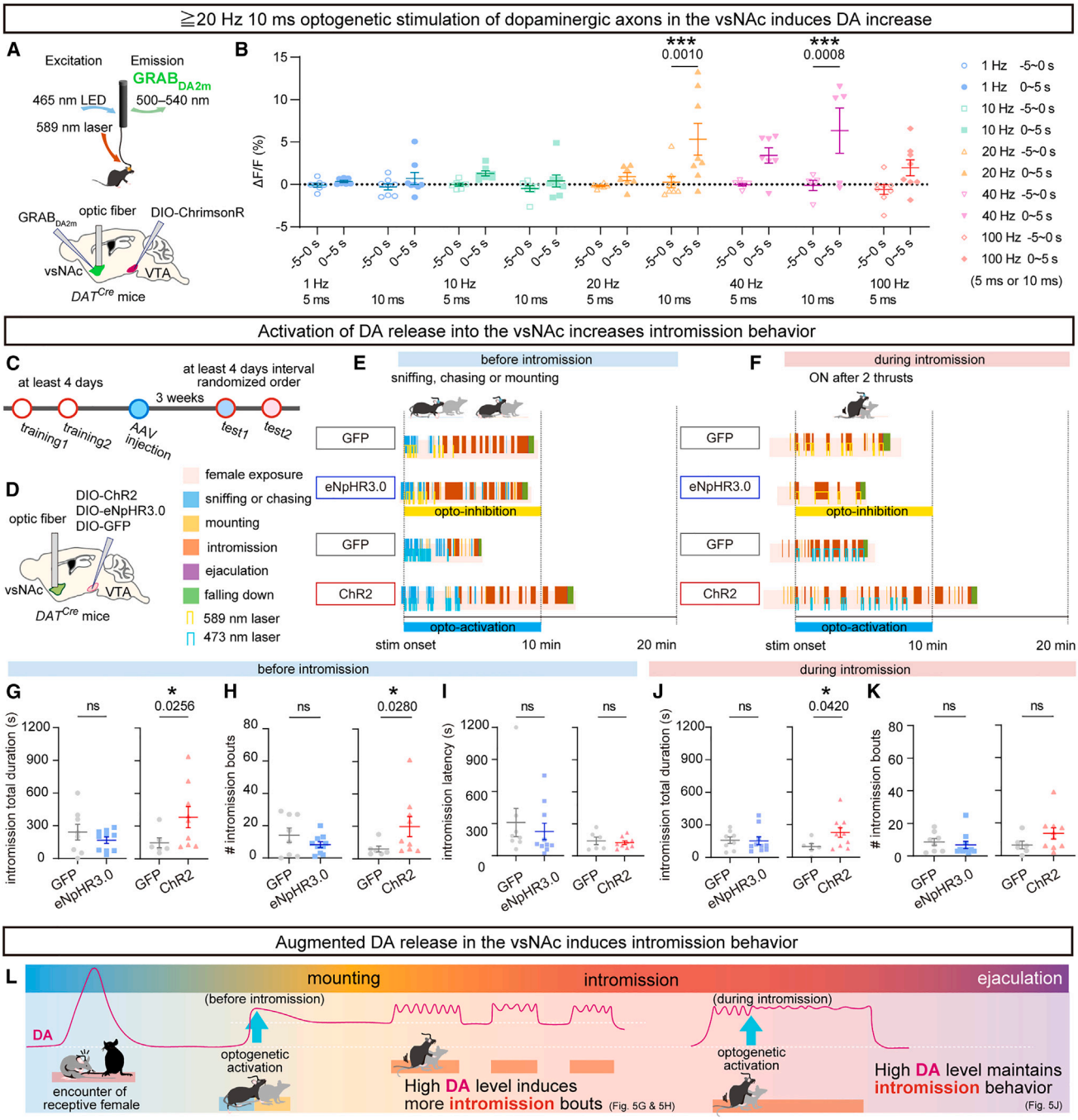

Figure 5. Optogenetic activation of DA release into the vsNAc increases intromission total duration

(A and B) The effects of optogenetic activation of $DA^{VTA \rightarrow vsNAc}$ axons on DA release in the vsNAc.

(A) Schematic demonstrating optogenetic manipulation of $DA^{VTA \rightarrow vsNAc}$ axons with fiber photometry $GRAB_{DA2m}$ imaging in the vsNAc.

(B) Quantitation of average ΔF/F of $GRAB_{DA2m}$ signals following optogenetic stimulation of $DA^{VTA \rightarrow vsNAc}$ axons with different frequencies ($n = 7$ [1 Hz 5 ms], 8 [1 Hz 10 ms], 7 [10 Hz 5 ms], 8 [10 Hz 10 ms], 7 [20 Hz 5 ms], 8 [20 Hz 10 ms], 7 [40 Hz 5 ms], 5 [40 Hz 10 ms], and 8 [100 Hz 5 ms] signals).

(C–K) The effects of optogenetic manipulation of $DA^{VTA \rightarrow vsNAc}$ axons on male sexual behavior.

(C) Experimental schedule.

(D) Schematic demonstrating optogenetic manipulation of $DA^{VTA \rightarrow vsNAc}$ axons (left). Behavioral ethograms and event labels for (E) and (F) (right).

(E and F) Illustration of sexual behavior and optogenetic manipulation of $DA^{VTA \rightarrow vsNAc}$ axons before (E) and during (F) intromission.

(G–I) The effects of optogenetic manipulation of $DA^{VTA \rightarrow vsNAc}$ axons before intromission ($n = 8$ GFP^{DA} vs. 10 $eNpHR3.0^{DA}$ mice; $n = 6$ GFP^{DA} vs. 9 $ChR2^{DA}$ mice) on the intromission total duration (G), the number of intromission bouts (H), and intromission latency (I).

(I) Intromission latency (s) = the 1st intromission onset − the 1st optogenetic stimulation onset.

(legend continued on next page)

Please cite this article in press as: Miyasaka et al., Sequential transitions of male sexual behaviors driven by dual acetylcholine-dopamine dynamics, Neuron (2025), https://doi.org/10.1016/j.neuron.2025.01.032

crucial role during intromission, we optogenetically manipulated the $DA^{VTA \rightarrow vsNAc}$ axon terminals to investigate whether changing DA dynamics in the vsNAc could affect male copulatory behaviors (Figures 5 and S6). We performed optogenetic stimulation of $DA^{VTA \rightarrow vsNAc}$ axons at 20 Hz (10 ms width) because optogenetic stimulation of $DA^{VTA \rightarrow vsNAc}$ axons at 1 or 10 Hz did not increase DA release (Figures 5A, 5B, S6A, and S6B). We bilaterally injected AAV-Ef1a-DIO-ChR2 or AAV-Ef1a-DIO-eNpHR3.0 into the VTA and inserted optic fibers into the vsNAc of DAT^{Cre} mice (Figure 5D). Notably, optogenetic activation of the $DA^{VTA \rightarrow vsNAc}$ axons either before intromission (during sniffing, chasing, or mounting) or during intromission (after two pelvic thrust movements) increased the total duration of intromission (Figures 5G and 5J). Additionally, optogenetic activation before intromission also increased the number of intromission bouts, although it did not immediately trigger intromission (Figures 5H and 5I). Conversely, optogenetic suppression of the $DA^{VTA \rightarrow vsNAc}$ axons before or during intromission did not affect male sexual behaviors (Figures 5G–5K and S6C–S6G), possibly owing to incomplete suppression of DA signaling (see discussion). These results suggest that a high level of DA signaling in the vsNAc promotes the initiation and maintenance of intromission (Figure 5L).

DA-mediated inhibition of $D2R^{vsNAc}$ neurons sustains male sexual behaviors, whereas suppression of $D1R^{vsNAc}$ neurons ensures forward progression of sexual behaviors

To elucidate how DA dynamics regulate the activities of D1R ($D1R^{vsNAc}$)- and D2R ($D2R^{vsNAc}$)-expressing neurons in the vsNAc during male sexual behaviors, we first confirmed the distribution of D1R and D2R in the NAc by *in situ* hybridization (Figures 6A–6C). The number of $D1R^{+}$ neurons was twice that of $D2R^{+}$ neurons in all subregions of the NAc (Figure 6B): 67.13% of DA receptor neurons in the vsNAc express *Drd1*, 30.26% express *Drd2*, and 2.60% express both (Figure 6C). Next, we unilaterally injected AAV-hSyn-DIO-GCaMP6s and inserted optic fibers in the vsNAc of *Drd1-Cre* ($Drd1^{Cre}$) and *Drd2-Cre* ($Drd2^{Cre}$) mice (Figures 6D–6F, S7A, and S7B). Fiber photometry recording revealed that the activities of both $D1R^{vsNAc}$ and $D2R^{vsNAc}$ neurons were suppressed during intromission (Figures 6E, 6F, S7A, and S7B), despite the opposite effects of D1R (excitatory) and D2R (inhibitory) signaling on neuronal activity.[45,46] The simplest explanation for this paradoxical observation is that DA signaling preferentially activates the D2R-mediated inhibition of neuronal activities during intromission owing to the different thresholds for D1R and D2R activation[15,51,52] (see discussion).

To study the functional importance of suppression of $D1R^{vsNAc}$ and $D2R^{vsNAc}$ neurons during intromission, we specifically expressed ChR2 in the $D1R^{vsNAc}$ or $D2R^{vsNAc}$ neurons by injecting AAV-Ef1a-DIO-ChR2 into the vsNAc of $Drd1^{Cre}$ or $Drd2^{Cre}$ mice, respectively (Figures 6G–6Q and S7C–S7F). While optogenetic activation of $D1R^{vsNAc}$ neurons before intromission did not affect male sexual behaviors, optogenetic stimulation of these neurons during intromission increased the total mounting duration by inducing repetitive mounting behaviors (Figures 6P and 6Q). Thus, the suppression of $D1R^{vsNAc}$ neurons during intromission is critical for ensuring the forward progression of male sexual behaviors.

On the other hand, optogenetic activation of $D2R^{vsNAc}$ neurons during sniffing, chasing, mounting, and intromission immediately stopped these sexual behaviors (Figures 6J, 6K, and 6N; Video S4). Consequently, optogenetic stimulation of $D2R^{vsNAc}$ neurons before intromission increased total mounting duration and prolonged ejaculation latency (Figures 6L and 6M). By contrast, optogenetic stimulation of $D2R^{vsNAc}$ neurons during intromission decreased total intromission duration by shortening the epoch duration of intromission (Figures 6N and S6F). These observations indicate that DA-mediated suppression of $D2R^{vsNAc}$ neurons is necessary for sustaining male sexual behaviors, including the maintenance of intromission (Figure 6R).

To summarize the functions of DA-mediated D1R/D2R signaling (Figure 6R), (1) augmented DA release in the vsNAc is observed at female exposure and during intromission, with higher levels at female exposure than those during intromission (Figures 1 and S1); (2) DA release at female exposure activates both $D1R^{vsNAc}$ and $D2R^{vsNAc}$ neurons (Figures S7A and S7B), which triggers mounting behavior (Figures 6I, 6P, and 6Q); and (3) DA release during intromission suppresses both $D1R^{vsNAc}$ and $D2R^{vsNAc}$ neurons (Figures 6E and 6F), which supports the maintenance of intromission (Figures 6I and 6N). The differential regulation of $D1R^{vsNAc}$ and $D2R^{vsNAc}$ neurons at female exposure and during intromission are presumably caused by the different threshold of DA-mediated D1R/D2R signaling (see discussion).

ACh signaling in the vsNAc promotes sequential transitions of intromission and ejaculation

To study how ACh signaling in the vsNAc regulates male sexual behaviors, we bilaterally injected AAV-Ef1a-DIO-ChR2 or AAV-Ef1a-DIO-eNpHR3.0 and inserted optic fibers into the vsNAc of $ChAT^{Cre}$ male mice (Figure 7A). Next, we optogenetically activated or inhibited the ChR2- or eNpHR3.0-expressing $ChAT^{vsNAc}$ neurons, respectively, before or during intromission and examined the effects on male copulatory behaviors (Figures 7B–7G and S8). While optogenetic activation of $ChAT^{vsNAc}$ neurons before intromission did not affect mating behaviors, optogenetic inhibition of $ChAT^{vsNAc}$ neurons before intromission significantly prolonged the latency of mounting, intromission, and ejaculation (Figures 7B, 7D, 7E, and S8A). These results suggest that ACh signaling in the vsNAc is required for the initiation of mounting, intromission, and ejaculation.

(J and K) The effects of optogenetic manipulation of $DA^{VTA \rightarrow vsNAc}$ axons during intromission (n = 8 GFP^{DA} vs. 10 $eNpHR3.0^{DA}$ mice; n = 6 GFP^{DA} vs. 10 $ChR2^{DA}$ mice) on the intromission total duration (J) and the number of intromission bouts (K).

(L) A model showing that enhancing DA release in the vsNAc before intromission increases intromission bouts while enhancing DA release during intromission prolongs intromission duration.

Mean ± SEM.

See also Figure S6 and Table S1. $^{*}p < 0.05$, $^{***}p < 0.001$.

Please cite this article in press as: Miyasaka et al., Sequential transitions of male sexual behaviors driven by dual acetylcholine-dopamine dynamics, Neuron (2025), https://doi.org/10.1016/j.neuron.2025.01.032

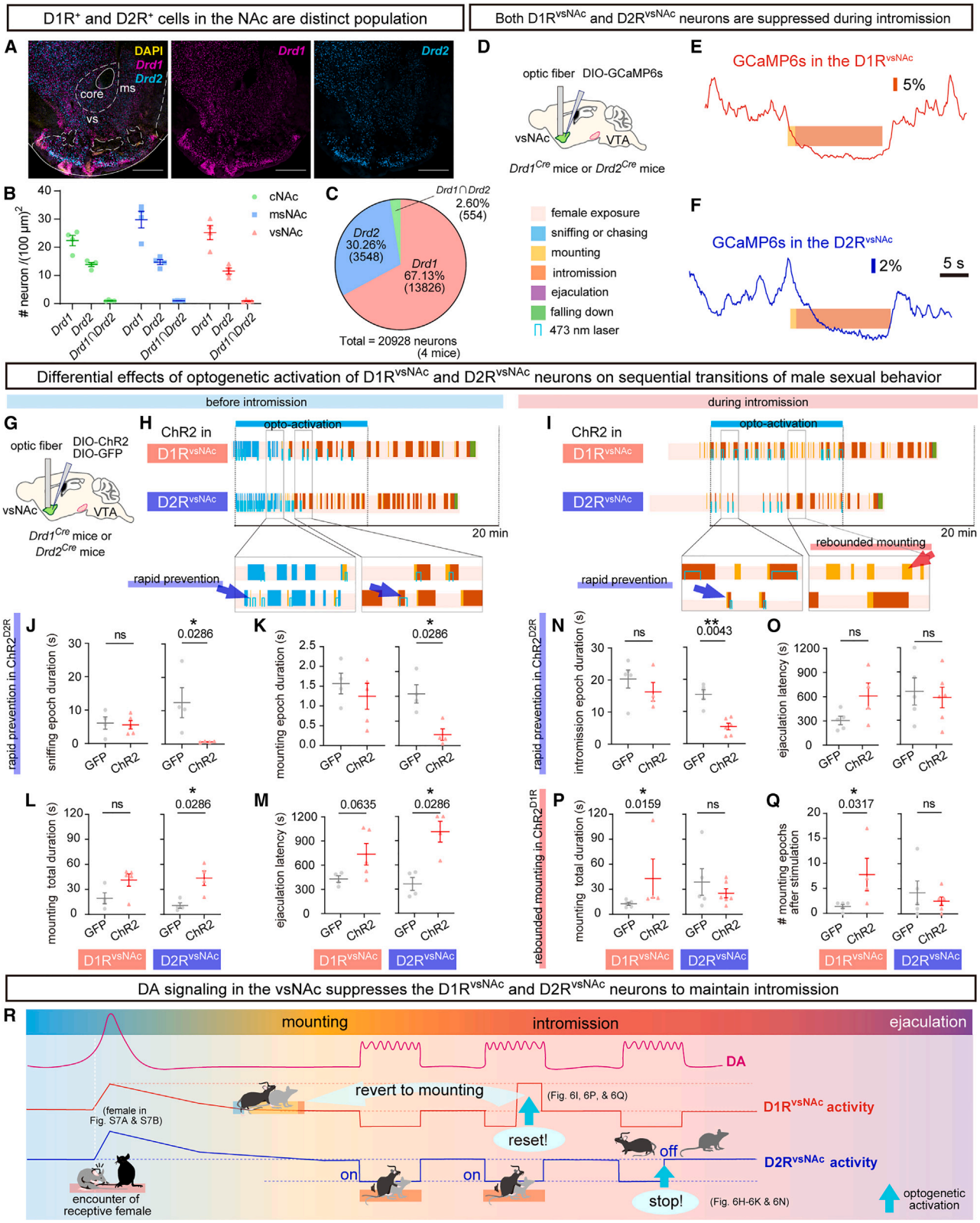

(legend on next page)

Please cite this article in press as: Miyasaka et al., Sequential transitions of male sexual behaviors driven by dual acetylcholine-dopamine dynamics, Neuron (2025), https://doi.org/10.1016/j.neuron.2025.01.032

Notably, optogenetic activation of ChAT^{vsNAc} neurons during intromission induced rapid ejaculation by shortening the ejaculation latency and increasing the likelihood of ejaculation (Figures 7C, 7F, and 7G; Video S5). Moreover, the number of mounting or intromission bouts and the total duration of mounting were also decreased (Figures S8G–S8I). By contrast, optogenetic inhibition of ChAT^{vsNAc} neurons during intromission did not affect mating behaviors (Figures 7F, 7G, S8G–S8J). These results indicate that the activation of ACh signaling in the vsNAc triggers the intromission-to-ejaculation transition.

To study how activation of ACh signaling changed DA dynamics during intromission, we injected AAV-hSyn-GRAB$_{DA2m}$ and AAV-Syn-FLEX-ChrimsonR into the vsNAc of *ChAT^{Cre}* mice and monitored DA dynamics by fiber photometry during optogenetic stimulation of ChAT^{vsNAc} neurons (Figures 7H–7J). Interestingly, optogenetic activation of ChAT^{vsNAc} neurons during intromission resulted in a decrease in the 1.5–2.2 Hz power of the DA rhythm followed by a brief suppression of DA release, which resembled the characteristic slowdown of DA rhythm just before ejaculation during IPE (Figures 2L, 2M, 7K and 7L). We observed stronger coherence between ACh-DA around IPE onset than those around IO onset (Figures S2M and S2N). These results suggest that the strong ACh-DA coherence in the vsNAc around IPE onset leads to an enhanced ACh release, which induces a slowdown of DA rhythm followed by immediate ejaculation (Figure 7M), possibly owing to a different ACh-DA modulatory mechanism such as via mAChRs in IPE compared with IO (see discussion).

DISCUSSION

Dual ACh-DA dynamics in the vsNAc drive sequential transitions of male copulatory behaviors

The neural mechanisms that regulate the sequential transitions of male copulatory behaviors, such as mounting, intromission, and ejaculation, remain unclear. Previous studies have identified specific brain regions that control mounting,[8–11] but the brain regions that regulate intromission and ejaculation are not known. Here, we identified the vsNAc as a critical brain region where dual ACh-DA dynamics align with and coordinate the sequential transitions from intromission to ejaculation. Our findings provide two significant advances in understanding the complex sequence of sexual behaviors: (1) patterning of neural activity during intromission is predictive of successful copulation and (2) activation of ChAT^{vsNAc} neurons increases the probability of advancing from intromission to ejaculation. In particular, the vsNAc exhibits a unique signature of 1.5–2.2 Hz dual ACh-DA rhythms that are concurrent with the pelvic thrust rhythm during intromission. The ACh rhythm, but not the DA rhythm, appears before the onset of intromission and persists during the short pauses of pelvic thrusting during intromission, suggesting that ACh rhythm is likely the primary driver for generating dual ACh-DA rhythms during intromission. We proposed that dual ACh-DA rhythms play a crucial role in the maintenance of intromission, possibly by reinforcing the pelvic thrust rhythm. By optogenetic manipulations of ACh and DA release in the vsNAc, we showed that ACh signaling promoted the initiation of intromission, whereas DA signaling was important for sustaining intromission through the suppression of D2R^{vsNAc} neurons. Furthermore, optogenetic activation of ChAT^{vsNAc} neurons during intromission elicits immediate ejaculation by triggering a slowdown of DA rhythm—a specific activity signature that typically precedes ejaculation during IPE. Taken together, these results demonstrate that dual ACh-DA dynamics harmonize in the vsNAc to drive the sequential transitions of male copulatory behaviors from intromission to ejaculation.

Dual ACh-DA rhythms are generated by reciprocal regulations between ACh and DA release

Both ChAT^{vsNAc} neurons and DA$^{VTA\rightarrow vsNAc}$ axons, but not DA^{VTA} somata, exhibited rhythmic neuronal activities during intromission, suggesting that the dual ACh-DA rhythms are regulated locally by mutual interaction between ChAT^{vsNAc} neurons and

Figure 6. Suppression of both D1R^{vsNAc} and D2R^{vsNAc} neurons during intromission is required to maintain intromission

(A) Representative image showing *in situ* hybridization of *Drd1* and *Drd2* mRNA in the NAc (scale bar, 500 μm).

(B) Quantification of neurons expressing *Drd1*, *Drd2*, or both in different subregions of the NAc (n = 4 mice/group).

(C) Pie chart showing the percentage of vsNAc neurons expressing *Drd1*, *Drd2*, or both.

(D) Schematic demonstrating fiber photometry GCaMP6s imaging in the D1R^{vsNAc} or D2R^{vsNAc} neurons of *Drd1^{Cre}* or *Drd2^{Cre}* mice (top). Behavioral ethograms and event labels for (E), (F), (H), and (I) (bottom).

(E and F) The neuronal activities of D1R^{vsNAc} (E) and D2R^{vsNAc} (F) neurons are suppressed during intromission.

(G) Strategy for optogenetic manipulation of D1R^{vsNAc} and D2R^{vsNAc} neurons.

(H and I) Illustration of sexual behavior and optogenetic manipulation of D1R^{vsNAc} or D2R^{vsNAc} neurons before (H) and during (I) intromission. Blue arrows indicate the rapid prevention of sexual behavior in ChR2^{D2R} mice, and red arrow shows rebounded mounting in ChR2^{D1R} mice.

(J–M) The effects of optogenetic activation of D1R^{vsNAc} (left) and D2R^{vsNAc} neurons (right) before intromission (n = 4 GFP^{D1R} vs. 5 ChR2^{D1R} mice; n = 4 GFP^{D2R} vs. 4 ChR2^{D2R} mice) on the epoch duration of sniffing (J), epoch duration of mounting (K), mounting total duration (L), and ejaculation latency (M).

(N–Q) The effects of optogenetic activation of D1R^{vsNAc} (left) and D2R^{vsNAc} neurons (right) during intromission (n = 5 GFP^{D1R} vs. 4 ChR2^{D1R} mice; n = 5 GFP^{D2R} vs. 6 ChR2^{D2R} mice) on the epoch duration of intromission (N), ejaculation latency (O), mounting total duration (P), and mounting bouts (Q).

(J, K, and N) Epoch duration (s) = the target behavior offset – the optogenetic stimulation onset.

(M and O) Ejaculation latency (s) = the ejaculation onset – the 1st optogenetic stimulation onset.

(Q) # mounting = the number of mounting behaviors observed during 10 min following the onset of optogenetic stimulation, excluding the mounting preceding intromission.

(R) A model showing that the highest level of DA release activates D1R^{vsNAc} and D2R^{vsNAc} neurons at female encounter, while high level of DA release suppresses both D1R^{vsNAc} and D2R^{vsNAc} neurons during intromission. Whereas optogenetic activation of D2R^{vsNAc} neurons rapidly stops any sexual behavior, the activation of D1R^{vsNAc} neurons during intromission reverts to repetitive mounting, presumably by mimicking the highest level of DA release at female encounter.

Mean ± SEM.

See also Figure S7, Table S1, and Video S4. *p < 0.05, **p < 0.01.

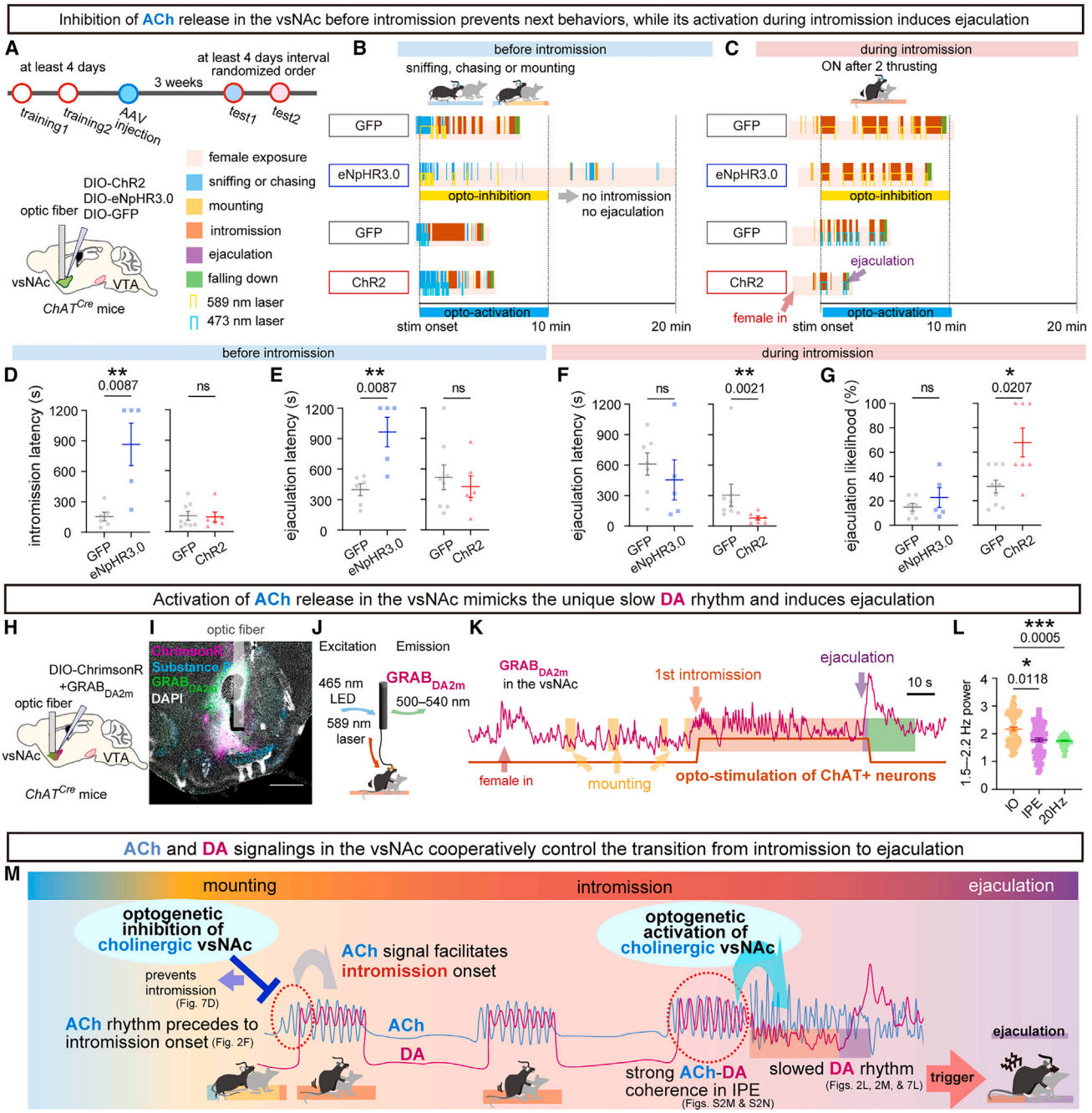

Figure 7. Optogenetic activation of ACh release into the vsNAc during intromission induces a specific slowdown of DA rhythm followed by immediate ejaculation

(A) Schematic of optogenetic manipulation of ChAT^{vsNAc} neurons. Behavioral ethograms and event labels for (B), (C), and (K) (bottom, right).

(B and C) Illustration of sexual behavior and optogenetic manipulation of ChAT^{vsNAc} neurons before (B) and during (C) intromission.

(D and E) The effects of optogenetic inhibition (left) and activation (right) of ChAT^{vsNAc} neurons before intromission (n = 6 GFP^{ACh} vs. 5 eNpHR3.0^{ACh} mice; n = 8 GFP^{ACh} vs. 6 ChR2^{ACh} mice) on the intromission latency (D) and ejaculation latency (E).

(F and G) The effects of optogenetic inhibition (left) and activation (right) of ChAT^{vsNAc} neurons during intromission (n = 7 GFP^{ACh} vs. 5 eNpHR3.0^{ACh} mice; n = 9 GFP^{ACh} vs. 7 ChR2^{ACh} mice) on the ejaculation latency (F) and ejaculation likelihood (G).

(D–F) Latency (s) = the 1st target behavior onset – the 1st optogenetic stimulation onset.

(G) Ejaculation likelihood (%) = ejaculation or not (1 or 0) in the test/# optogenetic stimulation.

(H–J) Schematic of surgery design (H), representative brain slice image (I), and recording system design (J) for simultaneous fiber photometry recording and optogenetic manipulation.

(legend continued on next page)

Please cite this article in press as: Miyasaka et al., Sequential transitions of male sexual behaviors driven by dual acetylcholine-dopamine dynamics, Neuron (2025), https://doi.org/10.1016/j.neuron.2025.01.032

$DA^{VTA \rightarrow vsNAc}$ axons. In support of this idea, we observed reciprocal regulations between ACh and DA release mediated by nAChR and D1R or D2R signaling in the NAc brain slices by *ex vivo* GRAB or GCaMP imaging combined with optogenetic and pharmacological manipulations. Computational modeling reveals that the dual ACh-DA rhythms in the vsNAc are generated by reciprocal ACh-DA regulations via D2R signaling in cholinergic neurons and D2R and nAChR signaling in dopaminergic axon terminals. Accordingly, knockdown of ChAT and D2R, but not D1R, expression in the vsNAc diminished the probability of sexual behaviors such as intromission and ejaculation. However, we could barely observe intromission in the D2R or ChAT (vsNAc) knockdown mice, making it difficult to verify the loss of dual ACh-DA rhythms during intromission. Thus, we performed *in silico* simulations to show that both D2R and ChAT are necessary for the generation of dual ACh-DA rhythms. Although we primarily focused on nAChR, D1R, and D2R to simplify our modeling of dual ACh-DA rhythms, we could not exclude a potential role for mAChRs in the generation of dual ACh-DA rhythms during intromission. Non-cholinergic $D1R^{vsNAc}$ and $D2R^{vsNAc}$ neurons may also contribute to the dual ACh-DA rhythms, a topic that warrants further investigation. A recent study also reported dual ACh-DA (~2 Hz) rhythms in the dorsal striatum during reward delivery, but these rhythms were not generated by direct interaction between ACh and DA release within the striatum,[31] suggesting that the dual ACh-DA rhythms can be generated by different mechanisms to regulate diverse biological processes.

Distinct functions of D1R and D2R signaling during male sexual behaviors

Our finding that both $D1R^{vsNAc}$ and $D2R^{vsNAc}$ neurons were suppressed during intromission is consistent with the proposed "threshold" hypothesis for D1R- and D2R-mediated DA signaling during sexual behaviors.[15,52] Since D2R has a higher affinity for DA than D1R,[51] DA signaling may preferentially cause the D2R-mediated suppression of $D2R^{vsNAc}$ neurons, while $D1R^{vsNAc}$ neurons are not activated during intromission (Figure 6R). Alternatively, it is plausible that suppression of $D2R^{vsNAc}$ neurons may indirectly lead to suppression of $D1R^{vsNAc}$ neurons through unknown mechanisms. For instance, we could not exclude a potential role for GABA release from dopaminergic neurons induced by cholinergic neurons.[53] Importantly, optogenetic activation of $D2R^{vsNAc}$ neurons either before or during intromission rapidly stopped sexual behaviors. It is possible that activation of $D2R^{vsNAc}$ neurons is associated with aversive emotions,[54,55] which may function as an "off" switch to pause male sexual behaviors. Thus, the DA-mediated suppression of $D2R^{vsNAc}$ neurons is necessary for sustaining male sexual behaviors such as intromission.

On the other hand, the highest level of DA release in the vsNAc was observed at the onset of female encounter or during ejaculation, which might cause the activation of $D1R^{vsNAc}$ neurons to regulate the initiation and termination of male sexual behaviors. Optogenetic activation of $D1R^{vsNAc}$ neurons during intromission increased the total mounting duration by inducing repetitive mounting behavior. It is plausible that optogenetic stimulation of $D1R^{vsNAc}$ neurons mimics the activation of $D1R^{vsNAc}$ neurons at female encounter (Figure 6R), thus resetting the sexual behaviors. Therefore, the suppression of $D1R^{vsNAc}$ neurons during intromission ensures the forward progression of male sexual behaviors by preventing animals from returning to the previous behavioral sequences such as mounting.

ACh signaling regulates ejaculation timing by triggering a slowdown of DA rhythm

We observed a specific slowdown of DA rhythm just before ejaculation that coincides with a big surge of DA release during IPE. Accordingly, optogenetic activation of $ChAT^{vsNAc}$ neurons resulted in a similar slowdown of DA rhythm followed by immediate ejaculation. However, optogenetic inhibition of $DA^{VTA \rightarrow vsNAc}$ axons during intromission did not elicit ejaculation. In the striatum, cholinergic interneurons make monosynaptic or polysynaptic axo-axonic contact on DA^{VTA} axons.[33,43] The ACh released from cholinergic interneurons can evoke action potentials at the DA^{VTA} axons and promote DA release from proximal and distant DA axons via the action potential propagation.[32,34] Similarly, optogenetic activation of $ChAT^{vsNAc}$ neurons may have a larger effect on DA dynamics in the vsNAc than direct optogenetic manipulation of $DA^{VTA \rightarrow vsNAc}$ axons. Moreover, optogenetic activation of $ChAT^{vsNAc}$ neurons results in a high level of ACh signaling, which then leads to a brief suppression of DA signaling, both of which may be required for inducing ejaculation.

It should be noted that pharmacological inhibition of mAChRs enhanced the release of DA following 1 or 10 Hz opto-stimulation of cholinergic neurons in the NAc brain slices, suggesting that mAChRs could suppress DA release in specific contexts of ACh signaling. Optogenetic stimulation of $ChAT^{vsNAc}$ neurons may cause a surge of ACh release, leading to the suppression of DA release by activating the inhibitory mAChRs on DA^{VTA} axons. Similarly, we observed that the coherence of ACh-DA rhythms between 1–4 Hz frequency was significantly higher at IPE onset than at IO onset. This increased coherence of dual ACh-DA rhythms probably results in a higher level of ACh signaling, which in turn may cause the suppression of DA rhythm by activating the inhibitory mAChRs. Future studies are warranted to elucidate the detailed mechanism for why dual ACh-DA rhythms specifically result in the slowdown of DA rhythm and trigger the intromission-to-ejaculation transition during IPE.

(K) Representative $GRAB_{DA2m}$ trace during the sequential transitions of male sexual behaviors with opto-stimulation marked by the increase of orange line.
(L) Comparison of 1.5–2.2 Hz power in $GRAB_{DA2m}$ signals during 20 s before the intromission offset among IO, IPE, and intromissions with optogenetic stimulation of $ChAT^{vsNAc}$ neurons. n = 462 (IO w/o stimulation), 198 (IPE w/o stimulation), and 1,320 (intromissions with 20 Hz, 10 ms stimulation) bins from 5 mice.
(M) A model showing that the ACh rhythm appears before intromission and facilitates the initiation of intromission. Optogenetic inhibition of $ChAT^{vsNAc}$ neurons before intromission may prevent the onset of intromission. During IPE, a strong coherence of dual ACh-DA rhythms results in a high level of ACh release, which leads to a slowdown of DA rhythm followed by ejaculation. Optogenetic activation of $ChAT^{vsNAc}$ neurons during intromission may mimic the high level of ACh release, which triggers a slowdown of DA rhythm and ejaculation.
Mean ± SEM. See also Figure S8, Table S1, and Video S5. $^{*}p < 0.05$, $^{**}p < 0.01$, $^{***}p < 0.001$.

Our results reveal a crucial role of ACh signaling in regulating the timing of ejaculation in mammals. Premature ejaculation (PE) is a prevalent sexual disorder affecting approximately 20%–30% of sexually active men.[56] Moreover, PE has been observed in relatively high percentages in Parkinson's disease patients, which is thought to be the result of the medications and the disease itself, with DA signaling being the common contributing factor.[57] Selective serotonin reuptake inhibitors are also used to treat patients with PE.[58] Although the exact mechanism is not yet fully understood, serotonin can affect the activity of DA neurons and DA release.[59–61] Therefore, these drugs may affect DA dynamics and, in turn, regulate ejaculation latency. We anticipate that our findings will be a starting point for more sophisticated studies into the molecular and neural mechanisms that govern ejaculation timing and the potential development of new therapeutics for sexual dysfunctions in humans.

RESOURCE AVAILABILITY

Lead contact

Requests for further information and resources should be directed to and will be fulfilled by the lead contact, Qinghua Liu (liuqinghua@nibs.ac.cn).

Materials availability

This study did not generate new reagents.

Data and code availability

- All data reported in this paper will be shared by the lead contact upon request.
- The code and dataset for NT modeling have been deposited at https://doi.org/10.5281/zenodo.12748185.
- The code and software used in this study are available from the lead contact upon request.
- Any additional information required to reanalyze the data reported in this paper is available from the lead contact upon request.

ACKNOWLEDGMENTS

We thank M. Jing for sharing reagents; A. Yoshida, M. Endo, N. Fujii-Sekine, T. Lou, and A. Watanabe for the behavioral analysis; Editage (www.editage.com) for language editing; and A. Ågmo, M. Yamamoto, and S. Inoue for valuable discussions. The graphical abstract was created with https://BioRender.com. This study was supported by JSPS KAKENHI (JP21J22555 and JP24K23231 to A.M.); JSPS KAKENHI Grant-in-Aid for Scientific Research on Innovative Areas, "Willdynamics" (JP19H05006 to K.S.); AMED under grant JP21zf0127005 (to Q.L.); the WPI program from Japan's MEXT; and the New Cornerstone Science Foundation.

AUTHOR CONTRIBUTIONS

Conceptualization, A.M., K.S., T.S., and Q.L.; methodology, A.M., K.S., Y.C., T.K., N.N., and J.S.; software, A.M., T.K., N.N., and J.S.; formal analysis, A.M. and T.K.; investigation, A.M., T.K., N.N., Y.T., Y.C., Y.I., and K.S.; resources, Y.L., J.S., M.Y., T.S., K.S., and Q.L.; writing – original draft, A.M. and Q.L.; writing – review & editing, A.M., T.K., N.N., Y.C., M.Y., H.T., A.H., K.S., T.S., and Q.L.; supervision, H.T., J.S., T.S., K.S., and Q.L.; funding acquisition, A.M., K.S., and Q.L.

DECLARATION OF INTERESTS

The authors declare no competing interest.

STAR★METHODS

Detailed methods are provided in the online version of this paper and include the following:

SUPPLEMENTAL INFORMATION

Supplemental information can be found online at https://doi.org/10.1016/j.neuron.2025.01.032.

Received: July 16, 2024
Revised: November 26, 2024
Accepted: January 31, 2025
Published: March 3, 2025

REFERENCES

1. Everitt, B.J. (1990). Sexual motivation: A neural and behavioural analysis of the mechanisms underlying appetitive and copulatory responses of male rats. Neurosci. Biobehav. Rev. *14*, 217–232. https://doi.org/10.1016/S0149-7634(05)80222-2.
2. Ågmo, A. (1997). Male rat sexual behavior. Brain Res. Brain Res. Protoc. *1*, 203–209. https://doi.org/10.1016/S1385-299X(96)00036-0.
3. Pfaus, J.G., Kippin, T.E., and Centeno, S. (2001). Conditioning and Sexual Behavior: A Review. Horm. Behav. *40*, 291–321. https://doi.org/10.1006/hbeh.2001.1686.
4. Paredes, R.G., and Ågmo, A. (2004). Has dopamine a physiological role in the control of sexual behavior?: A critical review of the evidence. Prog. Neurobiol. *73*, 179–226. https://doi.org/10.1016/j.pneurobio.2004.05.001.
5. Hull, E.M., and Dominguez, J.M. (2007). Sexual behavior in male rodents. Horm. Behav. *52*, 45–55. https://doi.org/10.1016/j.yhbeh.2007.03.030.
6. Balthazart, J., and Ball, G.F. (2007). Topography in the preoptic region: differential regulation of appetitive and consummatory male sexual behaviors. Front. Neuroendocrinol. *28*, 161–178. https://doi.org/10.1016/j.yfrne.2007.05.003.
7. Beach, F.A. (1976). Sexual attractivity, proceptivity, and receptivity in female mammals. Horm. Behav. *7*, 105–138. https://doi.org/10.1016/0018-506X(76)90008-8.
8. Sano, K., Tsuda, M.C., Musatov, S., Sakamoto, T., and Ogawa, S. (2013). Differential effects of site-specific knockdown of estrogen receptor α in the medial amygdala, medial pre-optic area, and ventromedial nucleus of the hypothalamus on sexual and aggressive behavior of male mice. Eur. J. Neurosci. *37*, 1308–1319. https://doi.org/10.1111/ejn.12131.
9. Wei, Y.-C., Wang, S.-R., Jiao, Z.-L., Zhang, W., Lin, J.-K., Li, X.-Y., Li, S.-S., Zhang, X., and Xu, X.-H. (2018). Medial preoptic area in mice is capable of mediating sexually dimorphic behaviors regardless of gender. Nat. Commun. *9*, 279. https://doi.org/10.1038/s41467-017-02648-0.

10. Karigo, T., Kennedy, A., Yang, B., Liu, M., Tai, D., Wahle, I.A., and Anderson, D.J. (2021). Distinct hypothalamic control of same- and opposite-sex mounting behaviour in mice. Nature *589*, 258–263. https://doi.org/10.1038/s41586-020-2995-0.

11. Bayless, D.W., Davis, C.-H.O., Yang, R., Wei, Y., de Andrade Carvalho, V.M., Knoedler, J.R., Yang, T., Livingston, O., Lomvardas, A., Martins, G.J., et al. (2023). A neural circuit for male sexual behavior and reward. Cell *186*, 3862–3881.e28. https://doi.org/10.1016/j.cell.2023.07.021.

12. Domínguez-Salazar, E., Naser, H.F., and Velázquez-Moctezuma, J. (2014). D1-like antagonist blocks conditioned place preference induced by ejaculation in male rats. Behav. Brain Res. *269*, 15–19. https://doi.org/10.1016/j.bbr.2014.04.026.

13. Pitchers, K.K., Vialou, V., Nestler, E.J., Laviolette, S.R., Lehman, M.N., and Coolen, L.M. (2013). Natural and Drug Rewards Act on Common Neural Plasticity Mechanisms with ΔFosB as a Key Mediator. J. Neurosci. *33*, 3434–3442. https://doi.org/10.1523/JNEUROSCI.4881-12.2013.

14. Beny-Shefer, Y., Zilkha, N., Lavi-Avnon, Y., Bezalel, N., Rogachev, I., Brandis, A., Dayan, M., and Kimchi, T. (2017). Nucleus Accumbens Dopamine Signaling Regulates Sexual Preference for Females in Male Mice. Cell Rep. *21*, 3079–3088. https://doi.org/10.1016/j.celrep.2017.11.062.

15. Hull, E.M., Eaton, R.C., Markowski, V.P., Moses, J., Lumley, L.A., and Loucks, J.A. (1992). Opposite influence of medial preoptic D1 and D2 receptors on genital reflexes: implications for copulation. Life Sci. *51*, 1705–1713. https://doi.org/10.1016/0024-3205(92)90299-5.

16. Hull, E.M., Eaton, R.C., Moses, J., and Lorrain, D. (1993). Copulation increases dopamine activity in the medial preoptic area of male rats. Life Sci. *52*, 935–940. https://doi.org/10.1016/0024-3205(93)90528-B.

17. Bitran, D., and Hull, E.M. (1987). Pharmacological analysis of male rat sexual behavior. Neurosci. Biobehav. Rev. *11*, 365–389. https://doi.org/10.1016/S0149-7634(87)80008-8.

18. Sun, F., Zeng, J., Jing, M., Zhou, J., Feng, J., Owen, S.F., Luo, Y., Li, F., Wang, H., Yamaguchi, T., et al. (2018). A Genetically Encoded Fluorescent Sensor Enables Rapid and Specific Detection of Dopamine in Flies, Fish, and Mice. Cell *174*, 481–496.e19. https://doi.org/10.1016/j.cell.2018.06.042.

19. Sun, F., Zhou, J., Dai, B., Qian, T., Zeng, J., Li, X., Zhuo, Y., Zhang, Y., Wang, Y., Qian, C., et al. (2020). Next-generation GRAB sensors for monitoring dopaminergic activity in vivo. Nat. Methods *17*, 1156–1166. https://doi.org/10.1038/s41592-020-00981-9.

20. Dai, B., Sun, F., Tong, X., Ding, Y., Kuang, A., Osakada, T., Li, Y., and Lin, D. (2022). Responses and functions of dopamine in nucleus accumbens core during social behaviors. Cell Rep. *40*, 111246. https://doi.org/10.1016/j.celrep.2022.111246.

21. Fiorino, D.F., and Phillips, A.G. (1999). Facilitation of sexual behavior and enhanced dopamine efflux in the nucleus accumbens of male rats after D-amphetamine-induced behavioral sensitization. J. Neurosci. *19*, 456–463. https://doi.org/10.1523/JNEUROSCI.19-01-00456.1999.

22. Holstege, G., Georgiadis, J.R., Paans, A.M.J., Meiners, L.C., van der Graaf, F.H.C.E., and Reinders, A.A.T.S. (2003). Brain Activation during Human Male Ejaculation. J. Neurosci. *23*, 9185–9193. https://doi.org/10.1523/JNEUROSCI.23-27-09185.2003.

23. Hull, E.M., Bitran, D., Pehek, E.A., Holmes, G.M., Warner, R.K., Band, L.C., and Clemens, L.G. (1988). Brain localization of cholinergic influence on male sex behavior in rats: Agonists. Pharmacol. Biochem. Behav. *31*, 169–174. https://doi.org/10.1016/0091-3057(88)90329-2.

24. Winn, P. (1991). Cholinergic stimulation of substantia nigra: effects on feeding, drinking and sexual behaviour in the male rat. Psychopharmacol. (Berl.) *104*, 208–214. https://doi.org/10.1007/BF02244180.

25. Pleim, E.T., Matochik, J.A., Barfield, R.J., and Auerbach, S.B. (1990). Correlation of dopamine release in the nucleus accumbens with masculine sexual behavior in rats. Brain Res. *524*, 160–163. https://doi.org/10.1016/0006-8993(90)90507-8.

26. Pfaus, J.G., Damsma, G., Nomikos, G.G., Wenkstern, D.G., Blaha, C.D., Phillips, A.G., and Fibiger, H.C. (1990). Sexual behavior enhances central dopamine transmission in the male rat. Brain Res. *530*, 345–348. https://doi.org/10.1016/0006-8993(90)91309-5.

27. Damsma, G., Pfaus, J.G., Wenkstern, D., Phillips, A.G., and Fibiger, H.C. (1992). Sexual behavior increases dopamine transmission in the nucleus accumbens and striatum of male rats: Comparison with novelty and locomotion. Behav. Neurosci. *106*, 181–191. https://doi.org/10.1037//0735-7044.106.1.181.

28. Coolen, L.M., Allard, J., Truitt, W.A., and McKenna, K.E. (2004). Central regulation of ejaculation. Physiol. Behav. *83*, 203–215. https://doi.org/10.1016/j.physbeh.2004.08.023.

29. Veening, J.G., and Coolen, L.M. (2014). Neural mechanisms of sexual behavior in the male rat: Emphasis on ejaculation-related circuits. Pharmacol. Biochem. Behav. *121*, 170–183. https://doi.org/10.1016/j.pbb.2013.12.017.

30. Hashikawa, K., Hashikawa, Y., Falkner, A., and Lin, D. (2016). The neural circuits of mating and fighting in male mice. Curr. Opin. Neurobiol. *38*, 27–37. https://doi.org/10.1016/j.conb.2016.01.006.

31. Krok, A.C., Maltese, M., Mistry, P., Miao, X., Li, Y., and Tritsch, N.X. (2023). Intrinsic dopamine and acetylcholine dynamics in the striatum of mice. Nature *621*, 543–549. https://doi.org/10.1038/s41586-023-05995-9.

32. Liu, C., Cai, X., Ritzau-Jost, A., Kramer, P.F., Li, Y., Khaliq, Z.M., Hallermann, S., and Kaeser, P.S. (2022). An action potential initiation mechanism in distal axons for the control of dopamine release. Science *375*, 1378–1385. https://doi.org/10.1126/science.abn0532.

33. Threlfell, S., Lalic, T., Platt, N.J., Jennings, K.A., Deisseroth, K., and Cragg, S.J. (2012). Striatal dopamine release is triggered by synchronized activity in cholinergic interneurons. Neuron *75*, 58–64. https://doi.org/10.1016/j.neuron.2012.04.038.

34. Wang, L., Shang, S., Kang, X., Teng, S., Zhu, F., Liu, B., Wu, Q., Li, M., Liu, W., Xu, H., et al. (2014). Modulation of dopamine release in the striatum by physiologically relevant levels of nicotine. Nat. Commun. *5*, 3925. https://doi.org/10.1038/ncomms4925.

35. Wang, L., Zhang, X., Xu, H., Zhou, L., Jiao, R., Liu, W., Zhu, F., Kang, X., Liu, B., Teng, S., et al. (2014). Temporal components of cholinergic terminal to dopaminergic terminal transmission in dorsal striatum slices of mice. J. Physiol. *592*, 3559–3576. https://doi.org/10.1113/jphysiol.2014.271825.

36. Beier, K.T., Steinberg, E.E., DeLoach, K.E., Xie, S., Miyamichi, K., Schwarz, L., Gao, X.J., Kremer, E.J., Malenka, R.C., and Luo, L. (2015). Circuit Architecture of VTA Dopamine Neurons Revealed by Systematic Input-Output Mapping. Cell *162*, 622–634. https://doi.org/10.1016/j.cell.2015.07.015.

37. Al-Hasani, R., McCall, J.G., Shin, G., Gomez, A.M., Schmitz, G.P., Bernardi, J.M., Pyo, C.-O., Park, S.I., Marcinkiewcz, C.M., Crowley, N.A., et al. (2015). Distinct Subpopulations of Nucleus Accumbens Dynorphin Neurons Drive Aversion and Reward. Neuron *87*, 1063–1077. https://doi.org/10.1016/j.neuron.2015.08.019.

38. Poulin, J.-F., Caronia, G., Hofer, C., Cui, Q., Helm, B., Ramakrishnan, C., Chan, C.S., Dombeck, D.A., Deisseroth, K., and Awatramani, R. (2018). Mapping projections of molecularly defined dopamine neuron subtypes using intersectional genetic approaches. Nat. Neurosci. *21*, 1260–1271. https://doi.org/10.1038/s41593-018-0203-4.

39. Chen, R., Blosser, T.R., Djekidel, M.N., Hao, J., Bhattacherjee, A., Chen, W., Tuesta, L.M., Zhuang, X., and Zhang, Y. (2021). Decoding molecular and cellular heterogeneity of mouse nucleus accumbens. Nat. Neurosci. *24*, 1757–1771. https://doi.org/10.1038/s41593-021-00938-x.

40. Voorn, P., Gerfen, C.R., and Groenewegen, H.J. (1989). Compartmental organization of the ventral striatum of the rat: Immunohistochemical distribution of enkephalin, substance P, dopamine, and calcium-binding protein. J. Comp. Neurol. *289*, 189–201. https://doi.org/10.1002/cne.902890202.

41. Jing, M., Li, Y., Zeng, J., Huang, P., Skirzewski, M., Kljakic, O., Peng, W., Qian, T., Tan, K., Zou, J., et al. (2020). An optimized acetylcholine sensor for monitoring in vivo cholinergic activity. Nat. Methods *17*, 1139–1146. https://doi.org/10.1038/s41592-020-0953-2.

42. Zhuo, Y., Luo, B., Yi, X., Dong, H., Miao, X., Wan, J., Williams, J.T., Campbell, M.G., Cai, R., Qian, T., et al. (2024). Improved green and red GRAB sensors for monitoring dopaminergic activity in vivo. Nat. Methods *21*, 680–691. https://doi.org/10.1038/s41592-023-02100-w.

43. Cachope, R., Mateo, Y., Mathur, B.N., Irving, J., Wang, H.-L., Morales, M., Lovinger, D.M., and Cheer, J.F. (2012). Selective Activation of Cholinergic Interneurons Enhances Accumbal Phasic Dopamine Release: Setting the Tone for Reward Processing. Cell Rep. *2*, 33–41. https://doi.org/10.1016/j.celrep.2012.05.011.

44. Jones, I.W., Bolam, J.P., and Wonnacott, S. (2001). Presynaptic localisation of the nicotinic acetylcholine receptor β2 subunit immunoreactivity in rat nigrostriatal dopaminergic neurones. J. Comp. Neurol. *439*, 235–247. https://doi.org/10.1002/cne.1345.

45. Neve, K.A., Seamans, J.K., and Trantham-Davidson, H. (2004). Dopamine receptor signaling. J. Recept. Signal Transduct. Res. *24*, 165–205. https://doi.org/10.1081/rrs-200029981.

46. Greif, G.J., Lin, Y.J., Liu, J.C., and Freedman, J.E. (1995). Dopamine-modulated potassium channels on rat striatal neurons: specific activation and cellular expression. J. Neurosci. *15*, 4533–4544. https://doi.org/10.1523/JNEUROSCI.15-06-04533.1995.

47. Cruz, H.G., Ivanova, T., Lunn, M.-L., Stoffel, M., Slesinger, P.A., and Lüscher, C. (2004). Bi-directional effects of GABAB receptor agonists on the mesolimbic dopamine system. Nat. Neurosci. *7*, 153–159. https://doi.org/10.1038/nn1181.

48. Galzi, J.L., Devillers-Thiéry, A., Hussy, N., Bertrand, S., Changeux, J.P., and Bertrand, D. (1992). Mutations in the channel domain of a neuronal nicotinic receptor convert ion selectivity from cationic to anionic. Nature *359*, 500–505. https://doi.org/10.1038/359500a0.

49. Fucile, S. (2004). Ca2+ permeability of nicotinic acetylcholine receptors. Cell Calcium *35*, 1–8. https://doi.org/10.1016/j.ceca.2003.08.006.

50. De Mei, C., Ramos, M., Iitaka, C., and Borrelli, E. (2009). Getting specialized: presynaptic and postsynaptic dopamine D2 receptors. Curr. Opin. Pharmacol. *9*, 53–58. https://doi.org/10.1016/j.coph.2008.12.002.

51. Richfield, E.K., Penney, J.B., and Young, A.B. (1989). Anatomical and affinity state comparisons between dopamine D1 and D2 receptors in the rat central nervous system. Neuroscience *30*, 767–777. https://doi.org/10.1016/0306-4522(89)90168-1.

52. Bazzett, T.J., Eaton, R.C., Thompson, J.T., Markowski, V.P., Lumley, L.A., and Hull, E.M. (1991). Dose dependent D2 effects on genital reflexes after MPOA injections of quinelorane and apomorphine. Life Sci. *48*, 2309–2315. https://doi.org/10.1016/0024-3205(91)90267-F.

53. Nelson, A.B., Hammack, N., Yang, C.F., Shah, N.M., Seal, R.P., and Kreitzer, A.C. (2014). Striatal Cholinergic Interneurons Drive GABA Release from Dopamine Terminals. Neuron *82*, 63–70. https://doi.org/10.1016/j.neuron.2014.01.023.

54. Lin, Y.-H., Yamahashi, Y., Kuroda, K., Faruk, M.O., Zhang, X., Yamada, K., Yamanaka, A., Nagai, T., and Kaibuchi, K. (2021). Accumbal D2R-medium spiny neurons regulate aversive behaviors through PKA-Rap1 pathway. Neurochem. Int. *143*, 104935. https://doi.org/10.1016/j.neuint.2020.104935.

55. Soares-Cunha, C., Coimbra, B., Sousa, N., and Rodrigues, A.J. (2016). Reappraising striatal D1- and D2-neurons in reward and aversion. Neurosci. Biobehav. Rev. *68*, 370–386. https://doi.org/10.1016/j.neubiorev.2016.05.021.

56. Raveendran, A.V., and Agarwal, A. (2021). Premature ejaculation - current concepts in the management: A narrative review. Int. J. Reprod. Biomed. *19*, 5–22. https://doi.org/10.18502/ijrm.v19i1.8176.

57. Bronner, G., Royter, V., Korczyn, A.D., and Giladi, N. (2004). Sexual Dysfunction in Parkinson's Disease. J. Sex Marital Ther. *30*, 95–105. https://doi.org/10.1080/00926230490258893.

58. Althof, S.E., McMahon, C.G., Waldinger, M.D., Serefoglu, E.C., Shindel, A.W., Adaikan, P.G., Becher, E., Dean, J., Giuliano, F., Hellstrom, W.J.G., et al. (2014). An Update of the International Society of Sexual Medicine's Guidelines for the Diagnosis and Treatment of Premature Ejaculation (PE). Sex. Med. *2*, 60–90. https://doi.org/10.1002/sm2.28.

59. Hillegaart, V., and Ahlenius, S. (1998). Facilitation and inhibition of male rat ejaculatory behaviour by the respective 5-HT1A and 5-HT1B receptor agonists 8-OH-DPAT and anpirtoline, as evidenced by use of the corresponding new and selective receptor antagonists NAD-299 and NAS-181. Br. J. Pharmacol. *125*, 1733–1743. https://doi.org/10.1038/sj.bjp.0702239.

60. Hull, E.M., Muschamp, J.W., and Sato, S. (2004). Dopamine and serotonin: influences on male sexual behavior. Physiol. Behav. *83*, 291–307. https://doi.org/10.1016/j.physbeh.2004.08.018.

61. Dremencov, E., El Mansari, M.E., and Blier, P. (2009). Effects of sustained serotonin reuptake inhibition on the firing of dopamine neurons in the rat ventral tegmental area. J. Psychiatry Neurosci. *34*, 223–229.

62. Lazarus, M., Shen, H.-Y., Cherasse, Y., Qu, W.-M., Huang, Z.-L., Bass, C.E., Winsky-Sommerer, R., Semba, K., Fredholm, B.B., Boison, D., et al. (2011). Arousal effect of caffeine depends on adenosine A2A receptors in the shell of the nucleus accumbens. J. Neurosci. *31*, 10067–10075. https://doi.org/10.1523/JNEUROSCI.6730-10.2011.

63. Schindelin, J., Arganda-Carreras, I., Frise, E., Kaynig, V., Longair, M., Pietzsch, T., Preibisch, S., Rueden, C., Saalfeld, S., Schmid, B., et al. (2012). Fiji: an open-source platform for biological-image analysis. Nat. Methods *9*, 676–682. https://doi.org/10.1038/nmeth.2019.

64. Rossi, J., Balthasar, N., Olson, D., Scott, M., Berglund, E., Lee, C.E., Choi, M.J., Lauzon, D., Lowell, B.B., and Elmquist, J.K. (2011). Melanocortin-4-receptors Expressed by Cholinergic Neurons Regulate Energy Balance and Glucose Homeostasis. Cell Metab. *13*, 195–204. https://doi.org/10.1016/j.cmet.2011.01.010.

65. Bäckman, C.M., Malik, N., Zhang, Y., Shan, L., Grinberg, A., Hoffer, B.J., Westphal, H., and Tomac, A.C. (2006). Characterization of a mouse strain expressing Cre recombinase from the 3' untranslated region of the dopamine transporter locus. Genesis *44*, 383–390. https://doi.org/10.1002/dvg.20228.

66. Inoue, S., Yang, R., Tantry, A., Davis, C., Yang, T., Knoedler, J.R., Wei, Y., Adams, E.L., Thombare, S., Golf, S.R., et al. (2019). Periodic Remodeling in a Neural Circuit Governs Timing of Female Sexual Behavior. Cell *179*, 1393–1408.e16. https://doi.org/10.1016/j.cell.2019.10.025.

67. Liu, C., Lee, C.-Y., Asher, G., Cao, L., Terakoshi, Y., Cao, P., Kobayakawa, R., Kobayakawa, K., Sakurai, K., and Liu, Q. (2021). Posterior subthalamic nucleus (PSTh) mediates innate fear-associated hypothermia in mice. Nat. Commun. *12*, 2648. https://doi.org/10.1038/s41467-021-22914-6.

68. Figueredo-Cardenas, G., Harris, C.L., Anderson, K.D., and Reiner, A. (1998). Relative Resistance of Striatal Neurons Containing Calbindin or Parvalbumin to Quinolinic Acid-Mediated Excitotoxicity Compared to Other Striatal Neuron Types. Exp. Neurol. *149*, 356–372. https://doi.org/10.1006/exnr.1997.6724.

69. Sun, Z., Wang, H.B., Deng, Y.P., Lei, W.L., Xie, J.P., Meade, C.A., Del Mar, N., Goldowitz, D., and Reiner, A. (2005). Increased calbindin-D28k immunoreactivity in striatal projection neurons of R6/2 Huntington's disease transgenic mice. Neurobiol. Dis. *20*, 907–917. https://doi.org/10.1016/j.nbd.2005.05.023.

70. Ishii, K.K., Osakada, T., Mori, H., Miyasaka, N., Yoshihara, Y., Miyamichi, K., and Touhara, K. (2017). A Labeled-Line Neural Circuit for Pheromone-Mediated Sexual Behaviors in Mice. Neuron *95*, 123–137.e8. https://doi.org/10.1016/j.neuron.2017.05.038.

71. Friard, O., and Gamba, M. (2016). BORIS: a free, versatile open-source event-logging software for video/audio coding and live observations.

Methods Ecol. Evol. *7*, 1325–1330. https://doi.org/10.1111/2041-210X.12584.

72. Ting, J.T., Daigle, T.L., Chen, Q., and Feng, G. (2014). Acute brain slice methods for adult and aging animals: application of targeted patch clamp analysis and optogenetics. Methods Mol. Biol. *1183*, 221–242. https://doi.org/10.1007/978-1-4939-1096-0_14.

73. Takahashi, T.M., Hirano, A., Kanda, T., Saito, V.M., Ashitomi, H., Tanaka, K.Z., Yokoshiki, Y., Masuda, K., Yanagisawa, M., Vogt, K.E., et al. (2022). Optogenetic induction of hibernation-like state with modified human Opsin4 in mice. Cell Rep. Methods *2*, 100336. https://doi.org/10.1016/j.crmeth.2022.100336.

74. Liu, C., Goel, P., and Kaeser, P.S. (2021). Spatial and temporal scales of dopamine transmission. Nat. Rev. Neurosci. *22*, 345–358. https://doi.org/10.1038/s41583-021-00455-7.

75. Akiba, T., Sano, S., Yanase, T., Ohta, T., and Koyama, M. (2019). Optuna: A Next-generation Hyperparameter Optimization Framework. In Proceedings of the 25th ACM SIGKDD International Conference on Knowledge Discovery & Data Mining KDD '19 (Association for Computing Machinery), pp. 2623–2631. https://doi.org/10.1145/3292500.3330701.

Please cite this article in press as: Miyasaka et al., Sequential transitions of male sexual behaviors driven by dual acetylcholine-dopamine dynamics, Neuron (2025), https://doi.org/10.1016/j.neuron.2025.01.032

STAR★METHODS

KEY RESOURCES TABLE

REAGENT or RESOURCE	SOURCE	IDENTIFIER
Antibodies		
chicken anti-GFP	Novus Biologicals	Cat #: NB100-1614; RRID:AB_10001164
rat anti-GFP	Nacalai Tesque	Cat #: 04404-84; RRID:AB_2313654
rat anti-Substance P	Merck & Co., Inc.	Millipore Cat #: MAB356; RRID:AB_94639
rabbit anti-Substance P	ImmunoStar Inc	Cat #: 20064; RRID:AB_572266
goat anti-mCherry	Sicgen	Cat #: AB0040-200; RRID: AB_2333092
rat anti-mCherry	Thermo Fisher Scientific	Cat #: M11217; RRID: AB_2536611
goat anti-ChAT	Merck & Co., Inc.	Millipore Cat #: AB144P; RRID: AB_207975
mouse anti-TH	Santa Cruz Biotechnology	Cat #: sc-25269; RRID: AB_628422
mouse anti-Calbidin-D-28K	Sigma-Aldrich	Cat #: C9848; RRID: AB_2314067
Sheep anti-Digoxigenin-POD	Roche Applied Science	Cat #: 11633716001; RRID: AB_514499
Sheep anti-Fluorescein-POD	Roche Applied Science	Cat #: 11426346910; RRID: AB_840257
Alexa Fluor 488 donkey anti-rat	Jackson ImmunoResearch Laboratories	Cat #: 712-545-153; RRID: AB_2340684
Alexa Fluor 488 donkey anti-rabbit	Jackson ImmunoResearch Laboratories	Cat #: 711-545-152; RRID: AB_2313584
Alexa Fluor 488 donkey anti-chicken	Jackson ImmunoResearch Laboratories	Cat #: 703-545-155; RRID: AB_2340375
Alexa Fluor 647 donkey anti-rat	Jackson ImmunoResearch Laboratories	Cat #: 712-605-153; RRID: AB_2340694
Alexa Fluor 647 donkey anti-rabbit	Jackson ImmunoResearch Laboratories	Cat #: 711-605-152; RRID: AB_2492288
Alexa Fluor 647 donkey anti-goat	Jackson ImmunoResearch Laboratories	Cat #: 705-605-147; RRID: AB_2340437
Alexa Fluor 647 donkey anti-goat	Thermo Fisher Scientific	Cat #: A-21447; RRID: AB_2535864
Cy3 donkey anti-rat	Jackson ImmunoResearch Laboratories	Cat #: 712-165-153; RRID: AB_2340667
Cy3 donkey anti-rabbit	Jackson ImmunoResearch Laboratories	Cat #: 711-165-152; RRID: AB_2307443
Cy3 donkey anti-goat	Jackson ImmunoResearch Laboratories	Cat #: 705-165-147; RRID: AB_2307351
Cy3 donkey anti-guinea pig	Jackson ImmunoResearch Laboratories	Cat #: 706-165-148; RRID: AB_2340460
Bacterial and virus strains		
pAAV-hsyn-DIO-GCaMP6s	William Wisden	Addgene: 184284; RRID: Addgene 184284
pAAV-hsyn-GRAB_DA2m	Yulong Li	Addgene: 140553; RRID: Addgene_140553
pAAV-hsyn-GRAB_ACh3.0	Yulong Li	Addgene: 121922; RRID: Addgene_121922
pAAV-hsyn-GRAB_rDA2m	Yulong Li	Addgene: 208700; RRID: Addgene_208700
pAAV-Syn-FLEX-rc[ChrimsonR-tdTomato]	Edward Boyden	Addgene: 62723; RRID: Addgene 62723
pAAV[shRNA]-CMV>mCherry-U6>Scramble_shRNA	VectorBuilder Inc. (Chicago, IL, USA)	The vector ID is VB010000-0024wah, which can be used to retrieve detailed information about the vector on vectorbuilder.com
pAAV[shRNA]- CMV>mCherry-U6>mChat[shRNA#1]	VectorBuilder Inc. (Chicago, IL, USA)	The vector ID is VB900124-3093ume, which can be used to retrieve detailed information about the vector on vector-builder.com
pAAV[shRNA]- CMV>mCherry-U6>mDrd1[shRNA#1]	VectorBuilder Inc. (Chicago, IL, USA)	The vector ID is VB221116-1384yaz, which can be used to retrieve detailed information about the vector on vectorbuilder.com
AAV10-H1-shScramble/CMV-mCHERRY	Lazarus et al.[62]	N/A

(*Continued on next page*)

Please cite this article in press as: Miyasaka et al., Sequential transitions of male sexual behaviors driven by dual acetylcholine-dopamine dynamics, Neuron (2025), https://doi.org/10.1016/j.neuron.2025.01.032

Continued

REAGENT or RESOURCE	SOURCE	IDENTIFIER
AAV10-H1-shDrd2/CMV-mCHERRY	This paper	The vector is designed in-house using BLOCK-iT™ RNAi Designer.
pAAV-hSyn-DIO-EGFP	Bryan Roth	Addgene: 50457; RRID: Addgene 50457
pAAV-EF1a-double floxed-hChR2(H134R)-EYFP-WPRE-HGHpA	Karl Deisseroth	Addgene: 20298; RRID: Addgene_20298
pAAV-Ef1a-DIO EYFP	Karl Deisseroth	Addgene: 27056; RRID: Addgene 27056
pAAV-Ef1a-DIO eNpHR3.0-EYFP	Karl Deisseroth	Addgene: 26966; RRID: Addgene 26966
Chemicals, peptides, and recombinant proteins		
AlexaFluor-594-cholera toxin subunit B	Thermo Fisher Scientific	Cat #: C34777
AlexaFluor-488-cholera toxin subunit B	Thermo Fisher Scientific	Cat #: C34775
NeuroTrace™ 435/455 Blue Fluorescent Nissl Stain	Invitrogen	Cat #: N21479
DAPI	Dojindo	Cat #: D523; CAS: 28718-90-3
NHS-Fluorescein	Thermo Fisher Scientific	Cat #: 46410
Biotinyl tyramide	chemodex	Cat #: B0270; CAS: 41994-02-9
NeutrAvidin Protein, DyLight™ 550	Thermo Fisher Scientific	Cat #: 84606
β-Estradiol (17β-Estradiol)	Nacalai Tesque	Cat #: 14541-74; CAS: 50-28-2
Progesterone	Nacalai Tesque	Cat #: 28921-51; CAS: 57-83-0
Sesame oil	Nacalai Tesque	Cat #: 25620-65; CAS: 8008-74-0
DHβE (Dihydro-β-erythroidine hydrobromide)	Tocris Bioscience	CAS: 29734-68-7
Atropine (Atropine Sulfate Monohydrate)	NACALAI TESQUE	CAS: 5908-99-6
Bromocriptine (2-Bromo-α-ergocryptine methanesulfonate salt)	Merck & Co., Inc.	CAS: 22260-51-1
SKF38398 (SKF 38393 hydrobromide)	Tocris Bioscience	CAS: 20012-10-6
Deposited data		
Computational modeling of ACh-DA signals during intromission	Zenodo	Zenodo: https://doi.org/10.5281/zenodo.12748185
Experimental models: Organisms/strains		
Mouse: C57BL/6J	CLEA Japan, Inc.	N/A
Mouse: B6;129S6-Chattm2(cre) Lowl/J (*ChAT*^{Cre} mouse)	The Jackson Laboratory	Stock # 006410; RRID: IMSR_JAX:006410
Mouse: B6.SJLSlc6a3tm1.1(cre) Bkmn/J (*DAT*^{Cre} mouse)	The Jackson Laboratory	Stock # 006660; RRID: IMSR_JAX:006660
Mouse: B6.FVB(Cg)-Tg(Drd1-cre)EY262Gsat/ Mmucd (*Drd1*^{Cre} mouse)	MMRRC originally from GENSAT BAC Tg project	Stock # 030989-UCD; RRID: MMRRC_030989-UCD
Mouse: B6.FVB(Cg)-Tg(Drd2-cre)ER44Gsat/ Mmucd (*Drd2*^{Cre} mouse)	MMRRC originally from GENSAT BAC Tg project	Stock # 032108-UCD; RRID: MMRRC_032108-UCD
Oligonucleotides		
Mouse Drd1 probe set (B1) set size: 20	Molecular Instruments	GenBank: NM_001291801
Mouse Drd2 probe set (B4) set size: 14	Molecular Instruments	GenBank: NM_010077.2
B1 488 HCR amplifier	Molecular Instruments	N/A
B1 647 HCR amplifier	Molecular Instruments	N/A
Software and algorithms		
Doric Neuroscience Studio	Doric Lenses Inc.	version 5. 4. 1. 5
MATLAB	Mathworks	R2022a
Fiji (ImageJ)	Schindelin et al.[63]	RRID: SCR_002285
Python	https://www.python.org/	3.7.2/3.9.6

(*Continued on next page*)

Please cite this article in press as: Miyasaka et al., Sequential transitions of male sexual behaviors driven by dual acetylcholine-dopamine dynamics, Neuron (2025), https://doi.org/10.1016/j.neuron.2025.01.032

Continued

REAGENT or RESOURCE	SOURCE	IDENTIFIER
Optuna	KDD '19: Proceedings of the 25th ACM SIGKDD International Conference on Knowledge Discovery & Data Mining	https://dl.acm.org/doi/10.1145/3292500.3330701
GraphPad Prism	GraphPad Software	9.4.1
R	R Project for Statistical Computing	RRID: SCR_001905
Andor iQ	Andor Technology	RRID: SCR_014461
Arduino UNO	https://www.arduino.cc/	N/A
Other		
TCS SP8 laser confocal microscope	Leica Microsystems GmbH	N/A
LSM800	Carl Zeiss AG	N/A
NanoZoomer XR	Hamamatsu Photonics	N/A
Axio Scan Z1	Carl Zeiss AG	N/A
Optical Fiber	KYOCERA Corporation	N/A
Logicool HD Webcam	Logitech International S.A.	C525r
FLIR USB3.0 Vision Camera	Teledyne FLIR	# CM3-U3-13Y3M-CS
vibratome	Leica	VT1200S; RRID: SCR_020243
EMCCD camera	Andor Technology	iXon Ultra 888
589 nm laser	Shanghai Laser	YL589T6-100FC
473 nm laser	Shanghai Laser	BL473T8-100FC
Pulse Stimulator	A.M.P.I.	Master-9
Digidata® 1440A Low-noise data acquisition system	Molecular Device	RRID: SCR_021038

EXPERIMENTAL MODEL AND STUDY PARTICIPANT DETAILS

Mice

All animal experiments were performed at the International Institute for Integrative Sleep Medicine, University of Tsukuba, in accordance with the guidelines for animal experimentation. The experiments were approved by the animal experiment committee of the institute and were conducted in accordance with NIH guidelines. Mice were given food and water *ad libitum* and maintained at a temperature of 23°C and relative humidity of 50%, with a 12-h light/12-h dark cycle. Male and female C57BL/6J mice (C57BL/6JJcl, CLEA Japan, Inc.), male *ChAT*^{Cre} mice (B6;129S6-Chattm2(cre)Lowl/J; ID# 006410, Jaxson Laboratory),[64] male *DAT*^{Cre} mice (B6.SJLSlc6a3tm1.1(cre)Bkmn/J; ID# 006660, Jaxson Laboratory),[65] male *Drd1*^{Cre} mice (B6.FVB(Cg)-Tg(Drd1-cre)EY262Gsat/Mmucd; ID# 030989-UCD from MMRRC originally from GENSAT BAC Tg project), and male *Drd2*^{Cre} mice (B6.FVB(Cg)-Tg(Drd2-cre)ER44Gsat/Mmucd; ID# 032108-UCD from MMRRC originally from GENSAT BAC Tg project) were used in this study. The ages of the mice used for the experiments were between 8 and 32 weeks.

METHOD DETAILS

Viruses

The plasmids used for AAV-hSyn-DIO-GCaMP6s (serotype 9), AAV-Syn-FLEX-rc[ChrimsonR-tdTomato] (serotype 1), AAV-hSyn-DIO-EGFP (serotype 9), AAV-EF1a-double floxed-hChR2(H134R)-EYFP-WPRE-HGHpA (serotype 9), AAV-Ef1a-DIO-EYFP (serotype 9), and AAV-Ef1a-DIO eNpHR3.0-EYFP (serotype 9) were purchased from Addgene. The plasmids used for AAV-CMV-mCherry/U6-Scramble_shRNA (shCtrl) (serotype 9), AAV-CMV-mCherry/U6-mChat (shChAT) (serotype 9), and AAV-CMV-mCherry/U6-*Drd1* (shD1R) (serotype 9) were purchased from vector-builder. AAV-H1-shScramble-4-CMV-mCHERRY (shCtrl) (serotype 10) and AAV-H1-shDrd2-4-CMV-mCHERRY (shD2R) (serotype 10) were shared by the University of Tsukuba. The plasmids used for AAV-hSyn-GRAB_DA2m ($GRAB_{DA2m}$) (serotype 9), AAV-hSyn-GRAB_ACh3.0 ($GRAB_{ACh3.0}$) (serotype 9), and AAV-hSyn-rDA2m ($GRAB_{rDA2m}$) (serotype 9) were provided by Yulong Li.

AAVs were prepared at the University of Tsukuba using the triple-transfection helper-free method and purified as previously described.[62] The titers of AAVs were determined by qPCR and purified viruses were stored in aliquots at -80°C. AAV titers were $9.79 \times 10^{11} - 6.24 \times 10^{14}$ genomic copies/mL.

Please cite this article in press as: Miyasaka et al., Sequential transitions of male sexual behaviors driven by dual acetylcholine-dopamine dynamics, Neuron (2025), https://doi.org/10.1016/j.neuron.2025.01.032

Stereotaxic surgery

Adult male mice (aged > 8 weeks) were stereotactically injected with AAVs and implanted with optical fibers after at least one week post AAV injection. The animals were anesthetized with isoflurane (2–4%) and placed in a stereotaxic frame (David Kopf Instruments, Tujunga, CA). Viruses were stereotactically delivered to the brains of mice at 2–5 months of age as described previously.[66] In brief, virus was delivered unilaterally (0.2 μL of AAV9-hSyn-GRAB$_{DA2m}$, AAV9-hSyn-DIO-GCaMP6s, AAV9-hSyn-GRAB$_{ACh3}$, and AAV9-hSyn-GRAB$_{rDA2m}$) or bilaterally (0.3 μL of AAV1-Syn-FLEX-rc[ChrimsonR-tdTomato], AAV9-hSyn-DIO-EGFP, AAV9-EF1a-double floxed-hChR2(H134R)-EYFP-WPRE-HGHpA, AAV9-Ef1a-DIO-EYFP, and AAV9-Ef1a-DIO-eNpHR3.0-EYFP).

To silence the gene expression of ChAT, D1R, or D2R, we bilaterally injected 0.2 μL of AAV9-CMV-mCherry/U6-shmChAT (GCTGAATGACATGTATCTAAA, shChAT), AAV9-CMV-mCherry/U6-shD1R (CTCTGCCCTACAACGAATAAT, shD1R), or AAV10-H1-shDrd2-CMV-mCherry (ACTCAGATGCTTGCCATTGTT, shD2R) into the vsNAc of C57BL/6J male mice. In the control group, AAV10-H1-shScramble-CMV-mCherry (GTCAGGCTATCGCGTATCG, shCtrl) or AAV9-CMV-mCherry-U6-shScramble (CCTAAGGT TAAGTCGCCCTCG, shCtrl) was injected bilaterally into the vsNAc of C57BL/6J male mice.

Immediately after surgery, mice were placed on a heated pad individually and then returned to their home cage following recovery from anesthesia. Animals were allowed at least 2 weeks of recovery in a reversed light/dark room following surgery prior to being tested in behavioral assays.

For retrograde tracing, we then injected 0.3 μL of the retrograde tracer cholera toxin subunit B (CTB) conjugated with AlexaFluor-594 (Thermo Fisher Scientific, C34777) and AlexaFluor-488 (Thermo Fisher Scientific, C34775) into the vsNAc and msNAc, respectively. Mice were perfused 5 days after CTB injection. Whole brain sections were prepared.

Immunohistochemistry

For histological analysis, animals were perfused with 4% paraformaldehyde (PFA) in 0.1 M phosphate-buffered saline (PBS, pH 7.4), and the brains were dissected and post-fixed overnight in 4% PFA. Coronal brain sections (60 μm) were prepared using a cryostat (Leica Biosystems, Nussloch, Germany) and immunostaining was performed as described previously.[67] In brief, sections were collected in PBS and were treated with permeabilization solution (1% Triton in PBS) at room temperature for 3 h, followed by incubation with the blocking buffer (10% Blocking One [Nacalai Tesque] and 0.3% Triton X-100 in PBS), and incubated overnight at 4°C using primary antibodies in the blocking buffer. For Calbindin-D-28K staining, sections were incubated with the primary antibody for 3 nights at 4°C.[68,69] After washing with PBS three times, brain slices were incubated with secondary (second) antibody in blocking buffer at 4°C overnight. The slices were stained with NeuroTrace fluorescent Nissl stain (Invitrogen, N21479) or 4',6-diamidino-2-phenylinodole (DAPI) (Dojindo, D523), washed, mounted, and coverslipped.

Primary antibodies used were as follows: chicken anti-GFP (Novus Biologicals; 1:4,000), rat anti-GFP (Nacalai Tesque; 1:2,000), rat anti-Substance P (Merck & Co., Inc.; 1:500), rabbit anti-Substance P (ImmunoStar Inc.; 1:1500), goat anti-mCherry (Sicgen; 1:2,000), rat anti-mCherry (Thermo Fisher Scientific; 1:500), goat anti-ChAT (Merck & Co., Inc.; 1:500), mouse anti-TH (Santa Cruz Biotechnology; 1:250), and mouse anti-Calbidin-D-28K (Sigma-Aldrich; 1:500).

Secondary antibodies used were as follows: Alexa Fluor 488 donkey anti-rat IgG (Jackson ImmunoResearch; 1:500), Alexa Fluor 488 donkey anti-rabbit IgG (Jackson ImmunoResearch; 1:500), Alexa Fluor 488 donkey anti-chicken IgG (Jackson ImmunoResearch; 1:500), Alexa Fluor 647 donkey anti-rat IgG (Jackson ImmunoResearch; 1:500), Alexa Fluor 647 donkey anti-rabbit IgG (Jackson ImmunoResearch; 1:500), Alexa Fluor 647 donkey anti-goat IgG (Jackson ImmunoResearch; 1:500), Alexa Fluor 647 donkey anti-goat IgG (Thermo Fisher Scientific; 1:1,000), Cy3 donkey anti-rat IgG (Jackson ImmunoResearch; 1:500), Cy3 donkey anti-rabbit IgG (Jackson ImmunoResearch; 1:500), Cy3 donkey anti-goat IgG (Jackson ImmunoResearch; 1:500), and Cy3 donkey anti-guinea pig IgG (Jackson ImmunoResearch; 1:500).

In situ hybridization

The cDNA fragments of mouse *Drd1*, *Drd2*, *Chrm1*, *Chrm2*, *Chrm3*, *Chrm4*, and *Chrm5* were amplified by PCR using antisense primers containing the T7 promoter sequence. *In vitro* transcription was performed with PCR-amplified templates using T7 RNA polymerase (Hoffman La Roche AG, Basel, Switzerland) to synthesize antisense RNA probes (Table S2). Two-color *in situ* hybridization was performed as previously described.[70] Briefly, the mice were deeply anesthetized with isoflurane and transcardially perfused with ice-cold 10% sucrose in Milli-Q water, followed by ice-cold 4% PFA. The collected brain samples were post-fixed with 4% PFA at 4°C overnight, followed by displacement with 30% sucrose in PBS containing 0.1% diethylpyrocarbonate (DEPC) at 4°C overnight. Coronal brain sections (40 μm) were prepared using a cryostat (Leica Biosystems, Nussloch, Germany). Brain sections were treated with proteinase K (Roche), acetylated, and then incubated with hybridization buffer containing antisense RNA probes at 60°C for 16 h. After stringent washing, the brain sections were incubated with peroxidase (POD)-conjugated anti-Fluorescein antibody from sheep (Roche Applied Science, Germany; 1:2,000) or POD-conjugated anti-Digoxigenin antibody from sheep (Roche Applied Science, Germany; 1:500) at 4°C overnight. To sequentially use a POD-conjugated antibody, a 2% sodium azide solution was used to inactivate HRP. TSA systems (TSA-FITC and TSA-Biotin) and DyLight™ 550 conjugated NeutrAvidin Protein (Thermo Fisher Scientific; 1:500) were used to enhance mRNA signals (Figures 4I, 4J, 6A–6C, S3C–S3F, and S5A–S5D).

For HCR staining, HCR™ RNA-FISH was performed using reagents from Molecular Instruments. In brief, the sections were incubated in 70% Ethanol/PBS at 4°C for 1 h. After washing in DEPC-PBS, the sections were treated with proteinase K (Roche Applied Science, Germany) at 37°C for 30 min. The sections were then incubated in probe hybridization buffer for 30 min at 37°C for 30 min,

followed by incubation with a combination of D1R and D2R probes (Molecular Instruments) overnight at 37°C. After washing in HCR probe wash buffer and 5xSSCT, the sections were then incubated overnight at 25°C with appropriate hairpins conjugated with Alexa Fluor 488 and 647 to visualize hybridization signals. After washing in 2× SSC, the sections were stained with anti-ChAT antibody using typical immunostaining method (Figures 3F and 3G).

Analysis of the brain slice images

Imaging of brain sections was conducted using a TCS SP8 laser confocal microscope (Leica Microsystems GmbH, Wetzlar, Germany), LSM800 (Carl Zeiss AG, Oberkochen, Germany), NanoZoomer XR (Hamamatsu Photonics, Hamamatsu City, Japan), and Axio Scan Z1 (Carl Zeiss AG, Oberkochen, Germany). To confirm the AAV-infected sites in the fiber photometry (Figures 1, 2, 5, 6, 7, S1, S2, S6, and S7), RNAi silencing (Figures 4I–4K and S5A–S5F), and optogenetics experiments (Figures 5, 6, 7, and S6–S8), coronal brain sections were immunostained for substance P (SP).[40] The recording site was identified based on fiber tracking of the brain histological section sample. Each subregion of the NAc was defined as follows. While the cNAc shows a low level of SP expression, the msNAc and vsNAc are characterized by high levels of SP expression. Moreover, the msNAc is located on the medial side of the cNAc, and the vsNAc is sandwiched between the cNAc and the dense SP axons (ventral pallidum) (Figure 1C).

Quantification of mAChR1–5, Drd1, and Drd2 on ChAT^{vsNAc} and DA^{VTA} neurons in the brain slice images

To confirm the expression patterns of ChAT and dopamine receptors (*Drd1* and *Drd2*) in the NAc (Figure 3F), ChAT and *mAChR1–5* subtypes (*mAChR1*, *mAChR2*, *mAChR3*, *mAChR4*, and *mAChR5*) in the vsNAc (Figure S3C), TH (tyrosine hydroxylase) and *mAChR1–5* in the VTA (Figure S3D), and dopamine receptors in the NAc (Figure 6A), we manually annotated positive cells using a multi-point function and extracted the NAc subregions by polygon selection in ImageJ/Fiji.[63] The number of signals in each subregion was counted using schemes implemented in Python 3.7.2. Expression ratios were calculated based on the number of regions of each target marker. The *Drd1* or *Drd2* ratio in the ChAT^{vsNAc} neurons was calculated as the target marker (*Drd1* or *Drd2*)$^{+}$ChAT^{+} / ChAT^{+} (%) (Figure 3G). To calculate the *mAChR1–5* ratio in the ChAT^{vsNAc} neurons, the target marker (mAChR*1–5*)$^{+}$ChAT^{+} / ChAT^{+} (%) was calculated (Figure S3E). To calculate the *mAChR1–5* ratio in DA^{VTA} neurons, the target marker (mAChR*1–5*)$^{+}$TH^{+} / TH^{+} (%) was calculated (Figure S3F). The number of neurons / (100 μm)^2 in each subregion of the NAc were calculated as the total number of the target marker (*Drd1* or *Drd2*) / the area of the region (100 μm)^2 (Figure 6B). The mean values for each mouse are shown (Figures 3G, 6B, S3E, and S3F).

The shRNA-mediated knockdown in the vsNAc

To calculate the knockdown ratio of target marker by shRNA, we prepared three types of images in which shRNA (mCherry), the target marker (GFP: *Drd1, Drd2*, or ChAT), and DAPI were visualized around the vsNAc. The target^{+} (mCheery^{+}, GFP^{+}, or DAPI^{+}) somata were extracted from each image using OpenCV 4.5.5. First, cv2.medialBlur with a kernel size of 9 was applied to the image to reduce noise. Next, the histogram of the image was calculated using cv2.calcHist, and the peak of the histogram was obtained using scipy.signal.find_peaks with a distance of 5. V_{pk} was set to the pixel value corresponding to the maximum peak. The image was binarized with a threshold of V_{pk} minus 10, and the contours of the target^{+} somata were extracted by applying cv2.findContours to the binarized image. The mode and method were set to becv2.RETR_EXTERNAL and cv2.CHAIN_APPROX_SIMPLE, respectively. We selected the contours of DAPI and the target markers with areas between 10 and 200 in the images. The knockdown ratios were calculated from the region numbers of the target markers, shRNA, and DAPI. The shRNA knockdown ratio was calculated as the target marker (*Drd1, Drd2* or ChAT)$^{+}$shRNA^{+} / DAPI^{+}shRNA^{+} (%). The mean values for each mouse are shown in Figures 4I–4K.

Sexual behavior test

Hormone priming

Stimulus females in estrus were induced as described previously.[8] C57BL/6J female mice were ovariectomized at >8 weeks of age. One week after the surgery, β-Estradiol (Nacalai Tesque) dissolved in sesame oil (Nacalai Tesque) (10 μg/0.1 mL; EB) was administered to all female mice as a stimulus. More than 1 d after the first EB injection, all female mice were hormonally primed with subcutaneous injections of EB 48 and 24 h before testing, and they received progesterone (Nacalai Tesque) dissolved in sesame oil (500 μg/0.1 mL) 4–6 h before testing to ensure high sexual receptivity. Male mice were exposed to all female mice in their home cages. Female mice were examined for ejaculation using a copulatory plug. Female stimuli that experienced ejaculation one time were used in the sexual behavior test. Male mice were exposed to a different receptive female mouse from that used in the previous test.

Behavioral analysis

Sexual behaviors, including mounting, intromission, ejaculation, and falling, were analyzed based on videos obtained using cameras. The video frames were manually annotated with these sexual behaviors using BORIS.[71] The duration and number of mountings, intromissions, and ejaculations were recorded for each mouse. The latency of each behavior was calculated by subtracting the female exposure timing from the onset of each behavior. For optogenetic manipulation before intromission, appetitive behaviors, including sniffing and chasing a stimulus female mouse, were manually annotated (Figures 5E, 6H, and 7B).

Visualization of the intromission thrust movements

The body regions of two male and female mice during intromission were extracted using Python 3.7.2 and OpenCV 4.5.5. to visualize their thrusting movements. First, video frames with intromission behaviors were extracted from the original videos, and the intromission frames were then converted into grayscale images. Frames with excessively fast movements of mice, caused by factors such as

Please cite this article in press as: Miyasaka et al., Sequential transitions of male sexual behaviors driven by dual acetylcholine-dopamine dynamics, Neuron (2025), https://doi.org/10.1016/j.neuron.2025.01.032

female's rejection, were excluded from the analysis. Next, the contrast-limited adaptive histogram equalization (CLAHE) operator was applied to the grayscale images to improve their contrast (clipLimit = 2.0, tileGridSize = (3, 3)). The histogram of each CLAHE image was calculated using cv2.calcHist. The histogram had several pixel values with a height of 500 pixels. With V_{500} representing the minimum pixel value, the binarization operator was applied to the CLAHE image using threshold V_{500}. Conversely, the createBackgroundSubstractorMOG2 (BSMOG2) was applied to the grayscale images, and the median smoothing filter with a kernel size of 25 was applied to the BSMOG2 images. The binarized CLAHE images were multiplied by the smoothed BSMOG2 images, and black (zero) pixels were extracted from the multiplied images as mouse body regions (Figure 2G). The Z-scored lines of mouse body region sizes and the bottom point as thrusting behavior were plotted using MATLAB (Figure 2H). The accuracy of pelvic thrust detection by this method is ~93.4% from 106 events, which was calculated by side-by-side comparison (within ±0.25 s) of the thrusting events determined by human analysis vs. by software analysis of the dynamic changes in the body size of male and female mice.

Fiber photometry experiment

Fiber photometry recording

For fiber photometry imaging of neurotransmitters, AAV9-hSyn-$GRAB_{DA2m}$, AAV9-hSyn-$GRAB_{ACh3.0}$, or AAV9-hSyn-$GRAB_{rDA2m}$ was injected unilaterally into the NAc of C57BL/6J mice. For fiber photometry imaging of Ca^{2+} dynamics, AAV9-hSyn-DIO-GCaMP6s was injected unilaterally into the VTA of DAT^{Cre} mice or the vsNAc of $ChAT^{Cre}$ mice, $Drd1^{Cre}$ mice, or $Drd2^{Cre}$ mice. More than 1 week after virus injection, a 200-μm core, 0.50 NA optical fiber (KYOCERA Corporation) was implanted unilaterally into the vsNAc or VTA. The mice were allowed to recover for at least 2 weeks before the experiments.

To monitor animal behavior during fiber photometry imaging, (method 1) a web camera (Logicool HD Webcam C525r, Logitech International S.A., Switzerland) was used. To synchronize the fiber photometry recording and the video recording that captures mouse behaviors, (method 2) a USB camera (FLIR USB3.0 Vision Camera # CM3-U3-13Y3M-CS; Teledyne FLIR, Wilsonville, OR) was used. The USB camera released the shutter at a rate of 10 fps based on the Fiber Photometry Console signals. On the day of the experiment, mice were recorded in their home cages with regular chow feeding for 2 h in the dark phase. More than 10 min after the onset of recording, an estrous female mouse was introduced into the home cage of the subject male mouse. The recording was stopped more than 2 h after introducing the female. After the test, we reviewed the video footage and examined the female mouse's vagina to identify any signs of ejaculation by the male mouse. In the two-color imaging of $GRAB_{ACh3.0}$, and $GRAB_{rDA2m}$, signals were collected from three sexual behavior tests (at least 6 d interval) (Figures 2A–2L and 4A–4G).

For DA, ACh, or GCaMP imaging, the fluorescence emitted by $GRAB_{DA2m}$, $GRAB_{ACh3.0}$, or GCaMP was excited by a blue LED (CLED465), and was filtered between 500 and 540 nm. The fluorescence emitted by $GRAB_{rDA2m}$ was excited by a green LED (CLED560) and was filtered between 580 and 680 nm. The $GRAB_{DA2m}$, $GRAB_{ACh3.0}$, and GCaMP signals were recorded at an acquisition rate of >10 Hz, and two-color imaging of $GRAB_{ACh3.0}$ and $GRAB_{rDA2m}$ were recorded at an acquisition rate of 20 Hz using Doric Neuroscience Studio (version 5.4.1.5, Doric Lenses Inc.). The LED output intensity was adjusted so that the light excitation of the optical fiber cable was approximately 30 $\mu W/mm^2$. The signals of $GRAB_{DA2m}$, $GRAB_{ACh3.0}$, and GCaMP between 500–540 nm and those of $GRAB_{rDA2m}$ between 580–680 nm were recorded.

Data analysis for fiber photometry signals

All fiber photometry signals, except for the two-color imaging of $GRAB_{ACh3.0}$ and $GRAB_{rDA2m}$, were transformed into 10 Hz by a MATLAB "interp1" function to align with the behavioral events. As peri-event time plots (PETP), to analyze the signal dynamics around the onset and offset of each sexual behavior, we extracted the signal intensities for 20 s before and after the behavioral events (for a total of 40 s). The ΔF/F ratio was calculated by dividing the signal intensity in each frame by the mean value for 20 s before the behavioral events. The ΔF/F ratio was z-scored against the extracted 40-s signal intensities. To compare the intensity changes of each signal, mean ΔF/F every 10 s in each behavioral event, in which the baseline was the mean for the first 10 s were plotted (Figures 1E–1G, S1G, S1H, S1J, S2E, S2H, S7A, and S7B).

To analyze the DA rhythm (Figures 1H–1J and 2M), ACh rhythm (Figures 2N and 2O), or dual ACh-DA rhythms (Figures 2E, 2K, 2L, and S2K) during intromission or mounting, we calculated the power spectrum using MATLAB FFT with a 3 s window shifted every 0.3 s or 0.25 s, respectively. To show that ACh rhythm, but not DA rhythm, started before intromission, we analyzed the sum of the power spectrum of the 1.5–2.2 Hz band of ACh/DA rhythms every 2 s observed from 10 s before to 10 s after the intromission onset (Figure 2F) and the mounting onset (Figure S2L). To analyze the ACh or DA rhythm during intromission, we collected the sum of the power spectrum every 0.2 Hz band during intromission behavior (Figures 2M–2O).

To analyze the coherence between $GRAB_{ACh3.0}$ and $GRAB_{rDA2m}$, first we prepared the extracted signals around intromission. The $GRAB_{ACh3.0}$ and $GRAB_{rDA2m}$ signals were extracted 20 s before the intromission onset to 10 s after the intromission onset and 10 s before the intromission offset to 10 s after the intromission offset (Figures 2B–2D, S2J, S2M–S2P). These two signals were combined, and 50 s length signals were prepared. Using these 50 s length signals, MATLAB wavelet coherence was applied. Average values of the wavelet coherence over all intromissions (Figure 2C), IO, and IPE (Figure S2M) were visualized by heatmap plot. To compare each frequency of coherence between $GRAB_{ACh3.0}$ and $GRAB_{rDA2m}$ around the intromission, we calculated the mean of the wavelet coherence around <1 Hz, 1–4 Hz, and >4 Hz every 10 s (Figures 2D and S2J). To compare the coherence between $GRAB_{ACh3.0}$ and $GRAB_{rDA2m}$ around the IO and IPE, the means of the wavelet coherence in IO and IPE around 1–4 Hz were calculated every 5 s (Figure S2N).

To examine the effect of sexual experience on the ACh-DA rhythms, a simple linear regression analysis was performed to assess the correlation between the number of sexual behavior test and the 1–4 Hz coherence between $GRAB_{ACh3.0}$ and $GRAB_{rDA2m}$ in the first 5 s of intromission bouts which exceeded more than 15 s (Figure S2O). Based on the simple linear regression analysis, the regression equation and the R^2 value were included in the figure to illustrate the model fit. The *p* value was also calculated to assess the statistical significance of the relationship.

To confirm whether the bout number of intromission affects ACh-DA coherence, we categorized the test sessions into two groups based on the number of intromission bouts: large number of intromission bouts (≧8 bouts) and small number of intromission bouts (<8 bouts). The mean wavelet coherence in large and small sessions around 1–4 Hz were calculated every 5 s (Figure S2P, top). To confirm whether each intromission epoch duration affect the coherence between $GRAB_{ACh3.0}$ and $GRAB_{rDA2m}$, the mean wavelet coherence around 1–4 Hz were calculated every 5 s in short (<10 s), medium (10–30 s), and long (>30 s) intromission epochs (Figure S2P, bottom).

To visualize ACh and DA dynamics in the vsNAc during each thrust in the intromission phase, we extracted the time point that showed the bottom of the area of the mouse body, which was assumed to be the pelvic thrusting behavior. Based on the bottom time point, we extracted $GRAB_{ACh3.0}$ and $GRAB_{rDA2m}$ around the thrusting behavior ± 0.5 s (Figures 2G–2I).

To analyze the $GRAB_{DA2m}$ dynamics with optogenetic activation of $DA^{VTA \rightarrow vsNAc}$ axons using ChrimsonR, the ΔF/F ratio was calculated by dividing the signal intensity in each frame by the mean value for 30 s before the stimulation onset (Figures 5B, S6A, and S6B). To compare the $GRAB_{DA2m}$ intensity before and after the stimulation, mean ΔF/F -5∼0 s and 0∼5 s around the stimulation onset were plotted (Figure 5B).

To analyze the $GRAB_{DA2m}$ dynamics with optogenetic activation of $ChAT^{vsNAc}$ neurons using ChrimsonR, we calculated the power spectrum using MATLAB FFT with a 3 s window shifted every 0.3 s and collected the power spectrum of the 1.5–2.2 Hz band observed from 20 s before the intromission offset to the intromission offset during intromission (Figure 7L).

Ex vivo imaging and optogenetics

We used 8- to 21-week-old $ChAT^{Cre}$ or $ChAT^{Cre}$; DAT^{Cre} male mice for imaging and optogenetic experiments during acute brain histological section preparation. These mice were injected with the following AAV vectors into the target brain areas at least 3 weeks prior to the experiments: (1) for imaging the DA response to photostimulation of cholinergic neurons in the vsNAc, AAV1-Syn-FLEX-ChrimsonR-tdTomato and AAV9-hSyn-$GRAB_{DA2m}$ were injected into the vsNAc of $ChAT^{Cre}$ mice (Figures 3B and 3C); (2) for imaging Ca^{2+} in cholinergic neurons in response to photostimulation of dopaminergic axons from the VTA, AAV1-Syn-FLEX-ChrimsonR-tdTomato and AAV9-hSyn-DIO-GCaMP6s were injected into the VTA and vsNAc of $ChAT^{Cre}$;DAT^{Cre} double transgenic mice, respectively (Figures 3D and 3E); (3) for imaging the ACh response to photostimulation of cholinergic neurons in the vsNAc, AAV1-Syn-FLEX-ChrimsonR-tdTomato and AAV9-hSyn-$GRAB_{ACh3.0}$ were injected into the vsNAc of $ChAT^{Cre}$ mice (Figures 3H–3K). Acute brain histological sections were prepared using a slightly modified N-methyl-d-glucamine (NMDG) protective recovery method.[72,73]

Briefly, mice were anesthetized with isoflurane and then cardiovascularly perfused with ice-cold NMDG-artificial cerebrospinal fluid (aCSF) consisting of 93 mM NMDG, 93 mM HCl, 2.5 mM KCl, 1.2 mM NaH_2PO_4, 30 mM $NaHCO_3$, 20 mM HEPES, 25 mM D-glucose, 5 mM Na-ascorbate, 2 mM thiourea, 3 mM Na-pyruvate, 10 mM $MgSO_4$, and 0.5 mM $CaCl_2$ (pH 7.4, adjusted with HCl, oxygenated with 95% O_2/5% CO_2). The brains were sliced to a thickness of 200 μm in ice-cold NMDG-aCSF using a vibratome (Leica VT1200S). Slices containing the striatum were incubated in NMDG-aCSF at 32°C for 12 min and then in HEPES-aCSF consisting of 124 mM NaCl, 2.5 mM KCl, 1.2 mM NaH_2PO_4, 24 mM $NaHCO_3$, 5 mM HEPES, 12.5 mM D-glucose, 2 mM $CaCl_2$, and 1 mM $MgSO_4$ (∼310 mOsm, oxygenated with 95% O_2/5% CO_2) at room temperature for at least 1 h. Slices were transferred into a chamber under an upright fluorescence microscope (Zeiss AxioExaminer D1, HXP120, water-immersion objective lens) and submerged in perfused HEPES-aCSF at 32–35°C. Fluorescence signals were acquired using an EM-CCD camera (Andor iXon Ultra 888, 1024 × 1024 pixels, 16 bit) and iQ software (Andor), in which green and red fluorescence were observed using a Zeiss filter set 38HE (excitation 470/40 nm, emission 525/50 nm) and Zeiss filter set 43 (excitation 545/25 nm, emission 605/70 nm), respectively. Green fluorescence included $GRAB_{DA2m}$, $GRAB_{ACh3.0}$, and GCaMP6s. The frame rate was 5 fps, except for experiments with Ca^{2+} imaging or bath application of SKF38398 (frame rate of 0.2 fps). Ca^{2+} imaging was performed with a 40x objective lens with a 0.5x zoom, while all other experiments were performed with a 20x lens with a 1.25x zoom. For optical stimulation, an optical fiber was placed just above the target area and outside the field of view, and optical stimuli (589 nm, 10-ms pulses for 30 s, Shanghai Laser) were controlled using a function generator (Master-9, AMPI). For pharmacological manipulation, nAChR antagonist DhβE (Dihydro-β-erythroidine hydrobromide, 1 μM), mAChR antagonist atropine (Atropine Sulfate Monohydrate, 2 μM), D2R agonist bromocriptine (2-Bromo-α-ergocryptine methanesulfonate salt, 15 μM), or D1R agonist SKF38398 (SKF 38393 hydrobromide, 100 μM) was used. A data acquisition system (Digidata® 1440A Low-noise data acquisition system, Molecular Devices) was employed to synchronize the timing of optical stimuli and image acquisition. This system allowed for precise monitoring of the timing of both processes.

Image analysis was performed using Fiji[63] and R. All images were subtracted from the background signal, which was the mean fluorescence intensity outside the field of view of the objective. Bleaching was corrected by linear interpolation of the medians of fluorescence intensity for 5–10 s before and after photostimulation. For optogenetics and imaging with $GRAB_{DA2m}$ or $GRAB_{ACh3.0}$, the edges of the 1024 × 1024-pixel images were removed to obtain 1008 × 1008-pixel images because the edges were outside the field of view of the objective lens. A total of 196 (16 × 16) square ROIs with 63 pixels per side were created in a 1008 × 1008

Please cite this article in press as: Miyasaka et al., Sequential transitions of male sexual behaviors driven by dual acetylcholine-dopamine dynamics, Neuron (2025), https://doi.org/10.1016/j.neuron.2025.01.032

image, and the mean fluorescence intensity within each ROI was calculated. ROIs without $GRAB_{DA2m}$ or $GRAB_{ACh3.0}$ expression (mean intensity <100) were excluded from the analysis. The mean fluorescence intensity was z-scored against the value obtained for 20 s before photostimulation. For experiments with SKF38398, bleaching was corrected using the median values for 60 s before and 120–180 s after bath application, and the fluorescence intensity was z-scored against the values for 60 s before the application. For Ca^{2+} imaging with GCaMP6s, ROIs were set on the somata of the neurons expressing GCaMP6s.

ROIs were classified using the Mann-Whitney U test, with values for 5 s before and 10 s after photostimulation for the GCaMP experiments (Figure 3E), and 60 s before and 120 s after the application of SKF38398 for the $GRAB_{ACh3.0}$ experiments (Figure 3K).

Computational modeling of DA and ACh dynamics

As we observed similar dynamics in GRAB and GCaMP ($GRAB_{DA2m}$ and GCaMP6s of dopaminergic axons in the vsNAc [Figures 1 and S1I–S1K], $GRAB_{ACh3.0}$ and GCaMP6s of cholinergic neurons in the vsNAc [Figures S2D–S2I]) by fiber photometry imaging, we hypothesized that (1) the neuronal activity of the neuronal ensemble reflects the amount of NT (neurotransmitter) released; (2) the GCaMP dynamics reflect the release probability of the NT. Based on these hypotheses, we developed a computational model to estimate the cellular environment in which neurons and receptors are involved in generating dual ACh-DA rhythms during intromission. In this model, we set neuronal assembly ($ChAT^{vsNAc}_{sim}$ and $DA^{VTA\rightarrow vsNAc}_{sim}$), the internal activity of neurons (release probability measurement, *RPM*), NT release (ACh_{sim} and DA_{sim}) based on the *RPM*, receptors expressed on neurons (D1R, D2R, and nAChR), and the extracellular environment in which the NT can be released. To mimic the change of the amount of the extracellular NT over time, in this model, we assumed the three steps of cycle: (1) the activation of target neurons by the external stimuli; (2) NT released from the target neurons; (3) the effect of the receptor by binding NT to the receptor on the target neurons. These cycles were repeated a certain number of times and, during this period, we recorded the *RPM* and amount of NT_{sim} released from the neurons which was determined based on the *RPM* value. Through this model, we attempted to estimate the appropriate cellular environment, including the type of receptors or neurons involved, by minimising $Diff(NT_{sim},NT_{real})$, the difference between the actual ACh-DA dynamics *in vivo* (NT recorded by fiber photometry: NT_{real}) and model-simulated ACh-DA dynamics (NT generated by the model: NT_{sim}) (Figures 4A, 4B, and S4A). As NT_{real}, we used typical rhythmic signals of *in vivo* $GRAB_{ACh3.0}$ and $rGRAB_{DA2m}$ during intromission from the data shown in Figures 2A–2L.

Hypothetical neurons and receptors used in this simulation were identified based on *ex vivo* imaging (Figure 3), the *in situ* hybridization results (Figures S3C–S3F), and previous reports.[50] As neurons and receptors, we placed D1R and D2R in $ChAT^{vsNAc}_{sim}$ neurons, as well as D2R and nAChR in $DA^{VTA\rightarrow vsNAc}_{sim}$ axon terminals. From our *ex vivo* imaging, we found that inhibitory mAChR may function as an autoreceptor (Figures 3B and 3C). However, since all subtypes of *mAChR* were expressed on $ChAT^{vsNAc}$ and DA^{VTA} neurons (Figures S3C–S3F), to simplify our modeling, we focused on D1R, D2R, and nAChR receptors in this experiment (Figure 4A). To simplify the model, the nAChR were defined as a baseline, and the characteristics, the *RS* and *RE* values, of D1R and D2R relative to the nAChR were explored (Figure 4B).

Activation of target neurons by the external stimuli

To mimic the cellular environment that neurons are activated by the external stimuli, in this modeling, we assumed that the *RPM* which reflects the intensity of neuronal activity was changed by the external stimuli or the effect of the receptor expressed on the neurons. *Activation* includes the spontaneous activity of the target neurons and stimulation of neurons by substances other than ACh and DA. Here, we defined that the *Activation* continuously adds a certain value to the target neuron. Thus, the value added as an external stimulus to the *RPM* of the target neurons every cycle was constant.

Release of NT from the target neurons

To mimic the manner of NT release, we defined that the volume of NT_{sim} released to the extracellular environment from the neurons was determined by the *RPM* value of the neurons. In this model, the volume of NT_{sim} released is equivalent to the *RPM* value if *RPM* is positive and 0 if *RPM* is negative (Figure 4B). Additionally, we defined the diffusion function of DA to mimic the *in vivo* extracellular DA diffusion mechanism.[74] The time course and intensity of the DA diffusion were investigated using this model (Figures S4B–S4D).

Effect of the receptor by binding NT to the receptor on the target neurons

Next, we considered the strategy to mimic the behavior of nAChR, D1R, and D2R. As reported in previous studies, DA receptors are GPCRs that are thought to respond more slowly than nAChR, the ionotropic receptor.[45–49] Incorporating these insights, we defined the characteristics of each receptor using two variables: *RE* (receptor efficacy), the effect intensity which changes *RPM*; *RS* (receptor speed), the latency where the *Receptor* function affects *RPM* from the time that NT_{sim} binds to the receptor. In this experiment, to simplify the setting, we set the nAChR related variables as constant values (nAChR's *RE* =1, and the *RS* =1), and estimated the characteristics of D1R and D2R by exploring their *RE* and *RS*. *RE* of D1R and D2R was searched over a range of positive values, and their *RS* was searched over a range of natural numbers.

For example, when ACh_{sim} binds to the nAChR expressed on the $DA^{VTA\rightarrow vsNAc}_{sim}$ axon terminals, the *RPM* of the $DA^{VTA\rightarrow vsNAc}_{sim}$ axon terminals increases by ACh_{sim} × 1 (nAChR's *RE* =1) one step later (nAChR's *RS* =1). Since the D1R receptor is an excitatory GPCR, we defined its operation as follows: when D1R receives DA_{sim}, "D1R's *RS*" step later, the *RPM* increases by DA_{sim} × "D1R's *RE*." By contrast, we defined operation of the D2R receptor, an inhibitory GPCR, receiving DA_{sim} as "D2R's *RS*" step later, *RPM* decreases by a factor of DA_{sim} × "D2R's *RE*". With these receptors' settings, we conducted computational modeling to estimate the *RE* and *RS* values.

To estimate receptor efficacy (*RE*) and receptor speed (*RS*) of DA receptors, we explored *RE* and *RS* values which minimise $Diff(NT_{sim},NT_{real})$, the difference between NT_{sim} and NT_{real} using Bayesian optimisation (Figure 4B). We used Optuna,[75] an automatic

Please cite this article in press as: Miyasaka et al., Sequential transitions of male sexual behaviors driven by dual acetylcholine-dopamine dynamics, Neuron (2025), https://doi.org/10.1016/j.neuron.2025.01.032

hyperparameter optimization software framework, to determine the best values for *RE* and *RS* using $Diff(NT_{sim}, NT_{real})$ as an indicator. We used the following values as a fixed value throughout exploration. The value added by *Activation* is 1. The number of trials conducted to estimate *RE* and *RS* of D1R and D2R was approximately 1,000 to 10,000, depending on the experimental design. In each experimental design, out of these trials, the one representing the smallest $Diff(NT_{sim}, NT_{real})$, the condition where NT_{sim} and NT_{real} are most similar, was used to define *RE* and *RS* of D1R and D2R. To express the effect speed of each receptor in seconds, the *RS* of each receptor and DA diffusion step were divided by 200, the sampling rate (Figures 4E and S4D).

Performance comparison by the different activation patterns

To prove which neurons should be activated in the generation of dual ACh-DA rhythms, we compared the $Diff(NT_{sim}, NT_{real})$ under the following three conditions: (1) $ChAT^{vsNAc}_{sim}$: on / $DA^{VTA\rightarrow vsNAc}_{sim}$: on (= $Activation_{(1,1)}$); (2) $ChAT^{vsNAc}_{sim}$: on / $DA^{VTA\rightarrow vsNAc}_{sim}$: off (= $Activation_{(1,0)}$); (3) $ChAT^{vsNAc}_{sim}$: off / $DA^{VTA\rightarrow vsNAc}_{sim}$: on (= $Activation_{(0,1)}$) (Figures 4D and S4A).

Estimation of RE and RS of dopamine receptors

To reveal the *RE* and *RS* values of D1R and D2R generating dual ACh-DA rhythms, we estimated the *RE* and *RS* values under the $Activation_{(1,1)}$ with full receptors condition (D1R and D2R on $ChAT^{vsNAc}_{sim}$, and D2R and nAChR on $DA^{VTA\rightarrow vsNAc}_{sim}$). We focused on trials showing the converged $Diff(NT_{sim}, NT_{real})$ because otherwise the trial indicated the failure of the variable search (Figures 4E and 4F).

Performance comparison by deletion of each candidate receptor

To find which candidate receptor is important for the generation of dual ACh-DA rhythms, we estimated the *RE* and *RS* values under five conditions which delete a target receptor; deletion of (1) D1R on $ChAT^{vsNAc}_{sim}$, (2) D2R on $ChAT^{vsNAc}_{sim}$, (3) D2R on $DA^{VTA\rightarrow vsNAc}_{sim}$, (4) D2R on both $ChAT^{vsNAc}_{sim}$ and $DA^{VTA\rightarrow vsNAc}_{sim}$, and (5) nAChR on $DA^{VTA\rightarrow vsNAc}_{sim}$. Then, we compared the $Diff(NT_{sim}, NT_{real})$ among these five conditions and the condition with full receptor using the estimated each candidate *RE* and *RS* of D1R and D2R (Figures 4G, S4E, and S4F).

Gene knockdown experiments

Sexual behavior test with shRNA treatment

Three weeks (±1 day) following AAV injection, male mice underwent the sexual behavior test once a week (±1 day) for 3 weeks. Male mice were relocated to the test room 30 min before starting the test. After the acclimation period, a female stimulus mouse was introduced into the home cage of a male subject mouse. Video recordings were conducted over the next 2 h. After the test, we reviewed the video footage and inspected the female mouse to determine whether the male mouse exhibited sexual behaviors. The intromission and ejaculation rates were then calculated based on the frequency of these behaviors observed across the three tests (Figures 4H, 4L, and 4M). Average latency, average number of bouts, and total duration of each behavior were calculated across the tests (Figures S5G–S5M). *In situ* hybridization and immunohistochemistry verified efficacy of knockdown of target gene expressions in the vsNAc (Figures 4I–4K and S5A–S5F).

Rotarod test with shRNA treatment

A rotarod test was conducted to confirm the motor coordination of mice expressing shRNA in the vsNAc. More than 3 weeks after the AAV injection, male mice were moved to the test room. After more than 15 min for room acclimation, we initiated a habituation process for the rotarod machine. During this phase, mice were placed in the stationary state of the rotarod machine for 2 min. After acclimatization, the male mice were allowed to practice on a rotarod for 2 min (14 rpm). Subsequently, we conducted three rotarod tests (each gradually increasing from 5 to 40 rpm for 300 s) (Figure 4H). We recorded the time until the mice were dropped from the rotarod machine. Between each test, the mice were allowed a 5-min break. The median value was plotted as an effect of motor coordination (Figure 4N).

Optogenetics experiments

To activate $DA^{VTA\rightarrow vsNAc}$ axons, $ChAT^{vsNAc}$ neurons, $D1R^{vsNAc}$ neurons, or $D2R^{vsNAc}$ neurons, AAV9-Ef1a-DIO-ChR2-EYFP, or AAV9-hSyn-DIO-EGFP was injected bilaterally into the VTA of DAT^{Cre} mice or the vsNAc of $ChAT^{Cre}$ mice, $Drd1^{Cre}$ mice, or $Drd2^{Cre}$ mice (Figures 5D, 6G, and 7A). To inhibit $DA^{VTA\rightarrow vsNAc}$ axon terminals or $ChAT^{vsNAc}$ neurons, AAV9-Ef1a-DIO-eNpHR3.0-EYFP or AAV9-Ef1a-DIO-EGFP was injected bilaterally into the VTA of DAT^{Cre} mice or the vsNAc of $ChAT^{Cre}$ mice (Figures 5D and 7A). After more than 2 weeks, 200-μm core and 0.50 NA optical fibers (KYOCERA Corporation) were bilaterally implanted into the vsNAc. The mice were allowed to recover for at least 2 weeks before conducting the experiments. The subjects were confirmed to exhibit sexual behavior two times before the test. The interval between each training was at least 4 days (Figures 5C and 7A). Ejaculation was determined by verifying the presence of a plug in the vagina of the female mouse. If male mice did not show any sexual behavior in 3 training trials, the mice were excluded. We performed optogenetic stimulation at 20 Hz (10 ms width) based on the results that optogenetic stimulation of $DA^{VTA\rightarrow vsNAc}$ axons at 1 or 10 Hz did not increase DA release (Figures 5A, 5B, S6A, and S6B).

On the test day, individual mice were moved to the experimental room 1 h before the experiments in the dark phase and were connected to an optic patch cable. The axonal terminals of dopaminergic neurons, D1R- and D2R-expressing neurons, and cholinergic neurons in the vsNAc were activated (473 nm, Shanghai Laser) or inhibited (589 nm, Shanghai Laser). We created a system to record the stimulation timing and manage the stimulation frequency using the Arduino UNO and Doric Neuroscience Studio. Video recordings and recordings of the optogenetic stimulation schedule were initiated simultaneously. In each test, the experimenter observed the behavior of the mice and turned on the switch to manually stimulate. The switch was immediately turned off if the target behavior was prevented. If the male mice did not exhibit any sexual behavior within 10 min of starting the test, the test was terminated and repeated on a different day. If the subject male mice did not ejaculate within 10 min after the onset of stimulation, we stopped the

Please cite this article in press as: Miyasaka et al., Sequential transitions of male sexual behaviors driven by dual acetylcholine-dopamine dynamics, Neuron (2025), https://doi.org/10.1016/j.neuron.2025.01.032

stimulation and confirmed the timing of ejaculation until 20 min after the onset of stimulation (Figure 7B). In our pilot experiment, we observed that most experienced mice (>2 times) show ejaculation within 20 min after female introduction, thus we waited for 20 min at least after the optogenetic stimulation onset. If the male mice did not show any sexual behavior within 10 min after the onset of the test, we stopped the test and retested it more than 4 d after the test. In the case that male mice did not show any sexual behavior in 5 tests, they were excluded.

Given the dynamic and variable nature of sexual behaviors, such as sniffing, mounting, and intromission, we simply defined two manipulation conditions–"before intromission" and "during intromission"–to assess the effects of optogenetic manipulations across distinct phases of sexual interaction (Figures 5C–5K, 6G–6Q, 7A–7G, S6C–S6H, S7C–S7F, and S8).

For optogenetic manipulations "before intromission", the laser (20 Hz, 10 ms) was turned on upon sniffing, chasing, and mounting. In the case when mounting was not prevented and transitioned to intromission, we immediately stopped the stimulation, and the timing of ejaculation was confirmed. In the case when the target behavior (sniffing, chasing, and mounting) was stopped by optogenetic manipulation, we turned off the stimulation and repeated the process until the mouse began intromission or until 10-min after the start of optogenetic manipulation. The timing of ejaculation was confirmed, and if the male mice did not ejaculate within 20 min after starting the optogenetic stimulation, the test was terminated, and the ejaculation latency was recorded as 1,200 s.

For optogenetic manipulations "during intromission," the laser (20 Hz, 10 ms) was turned on upon the first observed intromission episode, and repeated opto-stimulation during each subsequent intromission episode until ejaculation or within a 10-min period. When observing intromission, particularly more than two intromission-thrusting movements, the experimenter turned on the switch button to shine the laser. In cases where ejaculation was not observed within 10 min, the stimulation ceased, and we confirmed the timing of ejaculation was confirmed within 20 min from the first stimulation. If the male mice did not ejaculate within 20 min from the first stimulation, the test was terminated, and the ejaculation latency was recorded as 1,200 s.

Latency of each behavior was calculated by subtracting the 1st optogenetic stimulation onset from the onset of each 1st behavior (Figures 5I, 6M, 6O, 7D–7F, S6C, S6D, S6G, S7C, S7E, and S8A). Epoch duration of sniffing, mounting, and intromission were based on the optogenetic stimulation onset and the offset of each target behavior (Figures 6J, 6K, and 6N). For the scoring of rebounded mounting bouts by the optogenetic activation of D1R^{vsNAc} neurons during intromission, the mounting behaviors were counted during the 10 min from the optogenetic stimulation start. For its analysis, the mounting preceded to intromission were excluded (Figure 6Q). Ejaculation likelihood was delivered by dividing ejaculation number in the test (1 or 0) by the number of optogenetic stimulation (Figures 7G, S6D, and S6G).

Fiber photometry with optogenetics

To monitor DA dynamics when stimulating dopaminergic axons or cholinergic neurons, AAV9-hSyn-GRAB$_{DA2m}$ was injected into the vsNAc and AAV1-Syn-FLEX-ChrimsonR-tdTomato was injected in the VTA of *DAT^{Cre}* mice (Figures 5A, 5B, S6A, and S6B) or the vsNAc of *ChAT^{Cre}* mice (Figures 7H–7L). Subsequently, optical fibers with a 200-μm core and 0.50 NA (KYOCERA Corporation) were bilaterally implanted in the vsNAc. The mice were allowed to recover for at least 2 weeks before performing the experiments. GRAB$_{DA2m}$ recordings were conducted without optogenetics to confirm the GRAB$_{DA2m}$ signals. After confirmation, bilateral optogenetic manipulations without fiber photometry recordings were conducted to confirm optogenetic effects on sexual behavior. Target neurons were activated using a laser (589 nm, Shanghai Laser).

In the confirmation of DA release patterns with opto-stimulation of DA$^{VTA\rightarrow vsNAc}$ axons, we stimulated the DA$^{VTA\rightarrow vsNAc}$ axons of free-moving male *DAT^{Cre}* mice using 1, 10, 20, or 40 Hz frequency with 5 ms or 10 ms width laser stimulation (Figures 5A, 5B, S6A, and S6B). In the confirmation of DA release patterns with opto-stimulation of ChAT^{vsNAc} neurons during intromission, the experimenter observed the behavior of the mice. When observing intromission, particularly more than two intromission-thrusting movements, the experimenter turned on the switch button to shine the laser (20 Hz, 10 ms).

The LED output intensity was approximately 30 μW/mm^2. The GRAB$_{DA2m}$ signals within the 500–540 nm range were recorded (Figures 5A and 7J).

QUANTIFICATION AND STATISTICAL ANALYSIS

Recorded videos and histological samples were analyzed blind to relevant variables, including administrated solution, genotype, prior housing condition, surgical procedure, and virus injection. Videos were manually annotated using BORIS.[71] In particular, anogenital investigation (sniffing and chasing), mounting, repeated pelvic thrust (intromission), and ejaculation were scored for male sexual behaviors. After annotations, various parameters including latency, number, and duration were calculated for further analysis.

Data were processed and analyzed using MATLAB, R, Python 3.7.2, and GraphPad PRISM 9.4.1 (GraphPad Software, San Diego, CA). All results are expressed as mean ± SEM. Data of non-paired samples were analyzed with two-tailed non-parametric Mann-Whitney U test, Kruskal-Wallis test with Dunn's multiple comparisons test, or two-way ANOVA followed by Šídák's post hoc multiple comparison test. Data of paired samples were analyzed with Friedman's ANOVA followed by Dunn's multiple comparisons test. The significance threshold was held at $\alpha = 0.05$, two-tailed (not significant [ns], $p > 0.05$; *$p < 0.05$; **$p < 0.01$; ***$p < 0.001$; ****$p < 0.0001$). Details are available in Table S1.